RESEARCH ARTICLE

Dysregulation of intercellular communication in vitro and in vivo via extracellular vesicles secreted by pancreatic duct adenocarcinoma cells and generated under the influence of the AG9 elastin peptide-conditioned microenvironment

Lise Nannan[1,2,3] | Salomé Decombis[1,2] | Christine Terryn[4] | Sandra Audonnet[5] | Jean Michel[6] | Sylvie Brassart-Pasco[1,2] | Willy Gsell[3] | Uwe Himmelreich[3] | Bertrand Brassart[1,2]

[1]Université de Reims Champagne-Ardenne, Laboratoire de Biochimie Médicale et Biologie Moléculaire, UFR Médecine, Reims, France

[2]CNRS UMR 7369 Matrice Extracellulaire et Dynamique Cellulaire, Reims, France

[3]KU Leuven, Department of Imaging and Pathology, Biomedical MRI, Leuven, Belgium

[4]PICT Platform, University of Reims Champagne-Ardenne, Reims, France

[5]URCACyt Platform, University of Reims Champagne-Ardenne, Reims, France

[6]Inserm, Université de Reims Champagne-Ardenne, P3Cell UMR-S1250, SFR CAP-SANTE, Reims, France

Correspondence
Bertrand Brassart, Université de Reims Champagne-Ardenne, Laboratoire de Biochimie Médicale et de Biologie Moléculaire, UMR CNRS/URCA 7369 MEDyC, UFR Médecine, 51 Rue Cognacq Jay, 51095, Reims Cedex, France.
Email: bertrand.brassart@univ-reims.fr

Uwe Himmelreich and Bertrand Brassart are the co-last authors.

Abstract

Pancreatic ductal adenocarcinoma (PDAC) is an aggressive malignancy with poor prognosis due to its highly metastatic profile. Intercellular communication between cancer and stromal cells via extracellular vesicles (EVs) is crucial for the premetastatic microenvironment preparation leading to tumour metastasis. This study shows that under the influence of bioactive peptides derived from the extracellular matrix microenvironment, illustrated here by the AG-9 elastin-derived peptide (EDP), PDAC cells secrete more tumour-derived EVs. Compared to PDAC-derived EVs, tumour-derived EVs resulting from AG-9 treatment (PDAC AG-9-derived EVs) significantly stimulated cell proliferation. At constant amount, tumour-derived EVs were similarly taken up by PDAC and HMEC-1 cells. Tumour-derived EVs stimulated cell proliferation, migration, proteinase secretion, and angiogenesis. Bioluminescence imaging allowed tumour-derived EV/FLuc+ tracking in vivo in a PDAC mouse model. The biodistribution of PDAC AG-9-derived EVs was different to PDAC-derived EVs. Our results demonstrate that the microenvironment, through EDP release, may not only influence the genesis of EVs but may also affect tumour progression (tumour growth and angiogenesis), and metastatic homing by modifying the in vivo biodistribution of tumour-derived EVs. They are potential candidates for targeted drug delivery and modulation of tumour progression, and they constitute a new generation of therapeutic tools, merging oncology and genic therapy.

KEYWORDS
cancer progression, elastin-derived peptide, extracellular vesicle, microenvironment, pancreatic ductal adenocarcinoma

1 | INTRODUCTION

Pancreatic ductal adenocarcinoma (PDAC) accounts for 85%–90% of most malignant tumours of the pancreas. Its incidence is steadily increasing and it is expected to become the second leading cause of cancer death by 2030 (Rahib et al., 2014). The poor prognosis is due to late diagnosis. Most patients present metastatic dissemination. PDAC is characterised by an abundant desmoplastic stroma composed of extracellular matrix (ECM) proteins, various soluble factors and different cell types, such as cancer-associated fibroblasts (CAFs), pancreatic stellate cells (PSCs), endothelial cells and immune cells (Procacci et al., 2018). In this PDAC microenvironment, each cell type influences cancer development through the degradation of ECM macromolecules, including elastin fibres. These fibres are particularly abundant in elastic tissues such as arteries and lungs and mainly composed of elastin. Elastin is a fibrous protein of the ECM responsible for the structural integrity and function of tissues. Deposited only during the early stages of life, elastin is extremely stable and resistant and has a half-life of 70 years (Shapiro et al., 1991). However, its proteolysis by elastase-like proteases (matrix metalloproteinases [MMP], pancreatic elastase and leukocyte elastase) is linked to diseases affecting elastin-rich organs (Houghton et al., 2011; Lohmann et al., 1994). Elastin-derived peptides (EDPs) released under the action of elastase modulate cellular activities, through cell surface receptor binding, under both physiological and pathological conditions. Degradation of ECM leads to the release of bioactive ECM macromolecule fragments named matrikines (Maquart et al., 1999).

EDPs display a wide range of biological activities, influencing cell migration (Da Silva et al., 2018; Senior et al., 1980), differentiation (Betre et al., 2006), proliferation, chemotaxis (Da Silva et al., 2018, Long et al., 1988), tumour progression (Brassart et al., 2019; Donet et al., 2014; Huet et al., 2002; Toupance et al., 2012), angiogenesis (Robinet et al., 2005) and extracellular vesicle (EV) shedding (Brassart et al., 2019). Among all the EDPs described in the literature, xGxxPG and xGxPGxGxG consensus peptides are the most illustrated. In vivo study in melanoma and PDAC models showed that AGVPGLGVG (AG-9) EDP promotes tumour progression to a greater extent than VGVAPG (VG-6) EDP (Da Silva et al., 2018, Nannan et al., 2023). AG-9 peptide exerts its protumour activity through 37/67-kDa ribosomal protein SA (RPSA) binding on the cell surface (Da Silva et al., 2018). This protein, also referred to 67LR, LAMBR, LAMR1, lamR, LRP/LR, 37LRP, LBP, LBP/p40, NEM/1CHD4, SA, ICAS, and p40 is ubiquitously expressed. This is also a membrane receptor for pathogens, prions, and growth factors. Moreover, RPSA is involved in the assembly and/or stability of the 40S ribosomal subunit. The 37-, 53-, and 67 kDa forms are the major forms reported but additional high-molecular-weight (HMW) forms of 32, 37, 45, 53, 55, 67, 80, and >110 kDa were also reported. The conversion of the 37 kDa form to higher molecular weight species remains unclear (DiGiacomo & Meruelo, 2016). As for its distribution, RPSA is not only localized on the cell surface but also in the nucleus, in association with nucleolar pre-40S ribosomes, small nucleolar ribonucleoproteins (snoRNPs), chromatin, histones, and in the cytosol as a ribosomal component or as actin and cytoskeletal stress fibres partner. It was reported to mediate cell proliferation, adhesion, differentiation, invasion, and angiogenesis and also preventing cell apoptotic escape, allowing tumour progression (Vania et al., 2019). It has been very recently shown to be overexpressed in PDAC tissues and this overexpression was correlated to enhanced cell invasion, metastasis and poor prognosis (Wu et al., 2019).

As EDPs after elastolysis, EVs are naturally released into the extracellular microenvironment by most cell types and predominantly described in intercellular communication. Two major EV classes are relatively well described in this function: small EVs (exosomes) are small membranous vesicles of endocytic origin with a diameter of 30–150 nm, and large EVs (microvesicles) are membranous vesicles directly shed from the plasma membrane with a diameter of 50–5000 nm (Mathieu et al., 2019). Numerous studies have shown the biological roles of EVs in physio-pathological functions, such as immune and microbiological regulation, stem cell biology, cardiovascular diseases, neurodegenerative diseases, metabolic disorders and cancer progression (Al-Nedawi et al., 2008; Raposo & Stoorvogel, 2013, Taylor & Gerçel-Taylor, 2005). Their biogenesis is most likely linked to the extracellular environment and constraints. EVs contain cell-specific proteins, lipids, DNA, mRNAs, miRNAs and metabolites corresponding to EV membrane's or cargo's 'molecular signature,' which reflect activity/status of the parent cancer cells (Mathieu et al., 2019, Williams et al., 2019). Various cell types have been demonstrated to take up EVs of different cellular origins, but with different efficiencies (Gurung et al., 2021). EVs have tropism towards their cell origin (Wiklander et al., 2015). Tumour cells were reported to show higher uptake of tumour-derived EVs than stromal cells (Smyth et al., 2014). Preferential uptake of tumour-derived EVs by their parent cells was demonstrated in vitro and in vivo in different cancer models (Kim et al., 2017; Xu et al., 2020). It was reported that tumour-derived EVs determine organotropic metastasis (Hoshino et al., 2015) and their uptake by organ-specific cells prepare the premetastatic niche. Integrin expression pattern may predict organ-specific metastasis with the exosomal $\alpha 6\beta 4$ and $\alpha 6\beta 1$ integrins associated with lung targeting, while exosomal $\alpha v\beta 5$ integrin to liver targeting.

The dysregulation of EV biogenesis in different pathologies, especially cancer, was reported to be involved in tumour cell immune escape, therapy resistance, tumour growth, invasion and metastasis (Costa-Silva et al., 2015). However, no study investigating the influence of extracellular microenvironment, especially matrikines, on EVs tropism and on recipient cell biological activities were reported in the literature to date.

We previously demonstrated that EDPs including AG-9 were able to increase cell blebbing in fibrosarcoma cells (Brassart et al., 2019). As cell blebbing is involved in large vesicles generation, we were interested in the influence of AG-9 on PDAC cells

in terms of EV liberation (number and size), the EV content and the potential role in intercellular communication promoting tumour growth (Nannan et al., 2023) in mouse xenograft PDAC model.

2 | MATERIALS AND METHODS

2.1 | Elastin-derived peptides synthesis

The elastin-derived nonapeptide AG-9 (AGVPGLGVG) was synthesised and purified by ProteoGenix and then controlled for composition and purity through electrospray ionisation-mass spectrometry (ESI-MS) and HPLC.

2.2 | Cell culture

Human MIA PaCa-2/eGFP-FLuc$^+$ ductal pancreatic adenocarcinoma cells (Nannan et al., 2023) were cultured in high-glucose (4.5 g L^{-1}) Dulbecco's Modified Eagle's Medium (DMEM) (Gibco) supplemented with 10% heat-inactivated fetal bovine serum (FBS) (Sigma-Aldrich), 1% penicillin (final concentration, 50 U mL^{-1}; Gibco) and 1% streptomycin (final concentration, 50 U mL^{-1}; Gibco). Human HMEC-1 microvascular endothelial cells were cultured in the same condition with low-glucose (1 gL^{-1}) DMEM. Cells were cultured at +37°C under 5% CO$_2$ humid atmosphere. All the cell lines were confirmed to be mycoplasma free, based on routine PCR detection method.

2.3 | Antibodies and reagents

The following primary antibodies were used: rabbit anti-GM130 dilution of 1:1000 (western blot [WB], Cell Signaling Technology, 12480); mouse anti-CD63, dilution of 1:500 (WB) and 1:100 (TEM-immunogold labeling, Thermo Fisher Scientific, 10628D); rabbit anti-CD9, dilution of 1:1000 (WB, Abcam, ab92726); mouse anti-CD81, dilution of 1:1000 (WB, Santa Cruz Biotechnology, sc-166029); rabbit antiactin, dilution 1:3000 (WB, Sigma-Aldrich, a2066); mouse anti-GFP, dilution of 1:3000 (WB), 1:400 (immunofluorescence and flow cytometry) and 1:100 (TEM-immunogold labeling, Thermo Fisher Scientific, MA5-15256); rabbit anti-FLuc, dilution of 1:1 000 (WB), 1:400 (immunofluorescence and flow cytometry) and 1:100 (TEM-immunogold labeling, Abcam, ab21176); rabbit anti-RPSA, dilution of 1:1 000 (WB) and 1:100 (TEM-immunogold labeling, Abcam, ab99484); rabbit anti-ITGβ1, dilution of 1:1000 (WB, Abcam, ab52971); rabbit anti-ITGβ3, dilution of 1:1000 (WB, Abcam, ab119992); rabbit anti-MMP-14, dilution of 1:1000 (WB, Abcam, ab51074); rabbit anti-TRPM7, dilution of 1:1000 (WB, Abcam, ab109438). The following secondary antibodies were used: HRP-conjugated goat antimouse IgG (H+L) and HRP-conjugated goat antirabbit IgG (H+L), dilution of 1:10,000 (WB, GE Healthcare, NA931V and NA934V respectively); goat antimouse IgG H&L (10 nm Gold) and goat F(ab')$_2$ antirabbit IgG H&L (10 nm Gold), dilution of 1:50 (TEM-immunogold labeling, Abcam, ab39619 and ab39601 respectively); goat antimouse IgG (H+L) secondary antibody, Alexa Fluor 488 and goat antirabbit IgG (H+L) secondary antibody, Alexa Fluor 568, dilution of 1:1000 (immunofluorescence and flow cytometry, Invitrogen, A32731 and A11011, respectively).

2.4 | PDAC-derived EVs production and isolation

The MIA PaCa-2/eGFP-FLuc$^+$ cells were cultured in 150 cm^2 flasks in complete medium until 80%–90% confluence is reached. Cells were washed twice with PBS and incubated with or without AG-9 [10^{-7} M] in DMEM medium, without FBS, for 24 h. Conditioned media (CM) were collected and EVs were isolated via differential centrifugation protocol. A first centrifugation (Heraeus Multifuge X1R Centrifuge, Thermo Fisher Scientific) at 300 × g for 10 min at +4°C was carried out, followed a second centrifugation at 800 × g for 15 min at +4°C to remove cell debris and apoptotic bodies respectively. Then, CM were ultracentrifuged (Beckman Coulter) at 100,000 × g for 2 h at +4°C to pellet the EVs (namely PDAC-derived EVs or PDAC AG-9-derived EVs) using a Beckman Coulter Type 50.2 Ti Rotor. The EV pellets were washed with PBS, treated with size exclusion chromatography (EX01-25L Exo-spin Standard Kit, Cell Guidance Systems Ltd) according to the manufacturer instructions and ultracentrifuged (Optima TLX Ultracentrifugation Beckman Coulter) at 100,000 × g for 1 h at +4°C.

We have submitted all relevant data of our experiments to the EV-TRACK knowledgebase (EV-TRACK ID: EV230029) (Consortium et al., 2017).

2.5 | Western-blot analysis

Cells and EV pellets were lysed in RIPA lysis and extraction buffer (Sigma-Aldrich) supplemented with protease and phosphatase (Thermo Fisher Scientific) inhibitors. Proteins were quantified using the Pierce BCA Protein Assay Kit (Thermo Fisher Scientific). Subsequently, 20 μg of cell lysate proteins and 10 μg of EV proteins were loaded in Laemmli buffer on polyacrylamide gels and separated by SDS-PAGE. Proteins were then transferred onto polyvinylidene difluoride membranes (GE Healthcare Life Sciences). Membranes were incubated in a blocking solution of 5% bovine serum albumin (BSA) (Euromedex) in Tris buffer saline 0.1% Tween-20 (TBS-T) for 1 h at room temperature (RT). The membranes were incubated with primary antibodies overnight at +4°C in 1% BSA in TBS-T. The next day, the membranes were incubated with horseradish peroxidase-conjugated secondary anti-IgG antibodies at RT for 90 min in 1% BSA in TBS-T. Immunoreactive bands were revealed using ECL chemiluminescence detection kit (Amersham Biosciences, GE Healthcare Life Sciences). Acquisition and processing were obtained using the ChemiDoc MP imaging device and ImageLab (Bio-Rad Laboratories).

2.6 | RNA isolation and quantitative polymerase chain reaction with reverse transcription

Total RNAs from the indicated cells were isolated using the RNeasy Plus Mini Kit (Qiagen) according to the manufacturer's instructions. Before EV RNA extraction, EV-enriched pellets were treated with 4 μg mL^{-1} RNase A from bovine pancreas (Sigma-Aldrich) for 1 h at +37°C, to remove extravesicular RNAs. Quality and quantity of the isolated RNAs were evaluated using the Agilent system and 2100 bioanalyser software and the LVis plate and the SPECTROstar Nano spectrophotometer (BMG Labtech). Single-stranded cDNA was synthesised from 200 ng of RNA using a maxima first strand cDNA synthesis kit for RT-qPCR (Thermo Fisher Scientific). RT-quantitative PCR (qPCR) was performed using the maximum SYBR Green/ROX qPCR Master Mix (2X) (Thermo Fisher Scientific) using CFX Manager on a Bio-Rad CFX96 Real–Time system (Bio-Rad Laboratories). Target gene expression was normalised to the eukaryotic translation elongation factor 1 alpha 1 (*EEF1A1*) gene expression and was calculated using the $^{\Delta\Delta}$Ct method. Results were expressed as fold-change relative to untreated cells. Primers RT-qPCR oligonucleotide sequences are provided
in **Table 1**.

2.7 | Nanoparticle tracking analysis (NTA)

PDAC-derived EVs or PDAC AG-9-derived EVs were analysed for size and concentration using nanoparticle tracking analysis. Samples were diluted in PBS and analysis was performed on a NanoSight NS300 (Malvern Panalytical) system (camera Type: sCMOS; Laser Type Blue488; Camera level 15; Slider Shutter: 1206; Slider Gain: 245; FPS 25.0 and temperature set to +25°C). Three videos of 60 s were taken in light scatter mode with controlled fluid flow with a pump speed to 30 (arbitrary units). Videos were analysed using the batch analysis tool of NanoSight NTA software version 3.4 build 3.4.4 (video analysis settings (Detect Threshold: 5; Blur Size: Auto; Max Jump Distance: Auto: 13.0–14.4 pix). The average area under the histogram from the three videos was used for particle concentration measurement.

2.8 | Cell proliferation assay

MIA PaCa-2 and HMEC-1 cells (2×10^3 cells per well) were seeded in 96-well plates after enumeration of the viable cells using the Countness apparatus (Thermo Fisher Scientific) according to the Trypan blue exclusion test (EVE). Cells were grown in DMEM supplemented with 5% FBS. After 24 h, DMEM supplemented with 2.5% FBS with or without 10^9 PDAC-derived EVs or PDAC AG-9-derived EVs was added for 72 h. Cell proliferation was investigated using the WST-1 (Water-Soluble Tetrazolium-1, Roche) colorimetric assay according to the manufacturer's instructions. The absorbance was measured using a SPECTROstar Nano microplate spectrophotometer (BMG Labtech) at 450 nm.

2.9 | Long term growth assays

For long-term cell growth studies, MIA PaCa-2 cells were seeded at 10^4 cells mL^{-1} (5 mL) into a 25 cm^2 tissue-culture flask. EV pellets (cf., **PDAC-derived EVs production and isolation** paragraph) were resuspended in equal volumes of FBS-free culture medium (PDAC-derived EVs: 1.5×10^8 mL^{-1} and PDAC AG-9-derived EVs: 3×10^8 EVs mL^{-1}) and added to the 25 cm^2 tissue-culture flask. Cells were trypsinized 4 days later and counted. At each passage, 10^4 cells mL^{-1} were replated into a new 25 cm^2 culture flask with fresh medium containing PDAC EVs (PDAC-derived EVs: 1.5×10^8 mL^{-1} and PDAC AG-9-derived EVs: 3×10^8

TABLE 1　Primers used for the RT-qPCR analysis.

Gene	Primer	Sequence (5′ to 3′)	Company
ANXA1	F	TGA-ACT-TCG-TGC-TGC-CAT-GA	Eurofins
	R	CAC-GTT-TAC-GTC-TGT-CCC-CT	Genomics
CXCL8	F	TTC-TGC-AGC-TCT-GTG-TGA-AGG	Eurofins
	R	TCT-GCA-CCC-AGT-TTT-CCT-TGG	Genomics
eEF1A1	F	CTG-GAG-CCA-AGT-GCT-AAC-ATG-CC	Eurofins
	R	CCG-GGT-TTG-AGA-ACA-CCA-GTC	Genomics
EGFR	F	AGC-TAC-GGG-GTG-ACT-GTT-TG	Eurofins
	R	GTA-GTG-TGG-GTC-TCT-GCT-GG	Genomics
FLUC	F	TTC-GAC-CGG-GAC-AAA-ACC-AT	Eurogentec
	R	GGG-ATG-ATC-TGG-TTG-CCG-AA	
GFP	F	CGT-AAA-CGG-CCA-CAA-GTT-CAG	Eurogentec
	R	GCT-TCA-TGT-GGT-CGG-GGT-AG	
ITG αV	F	TTG-TTG-CTA-CTG-GCT-GTT-TTG	Eurofins
	R	TCC-CTT-TCT-TGT-TCT-TCT-TGA	Genomics
ITG α5	F	CCT-GAA-GAT-GCC-CTA-CCG-AA	Eurogentec
	R	ATC-CAC-AGT-GGG-ACG-CCA-TA	
ITG β1	F	AAC-TTG-TTG-GAA-AAC-AGC-GCA	Eurogentec
	R	CGG-CAT-CTG-TGG-AAA-ACA-CC	
ITG β3	F	GAC-AAG-GGC-TCT-GGA-GAC-AG	Eurogentec
	R	ACT-GGT-GAG-CTT-TCG-CAT-CT	
MMP 2	F	GCT-GGG-AGC-ATG-GCC-ATG-GAT-ACC	Eurogentec
	R	GGA-CAG-AAG-CCG-TAC-TTC-CCA-TCC	
MMP 14	F	ACG-CAT-TTG-GTC-GTA-TTG-GG	Eurogentec
	R	CGG-GTC-AGG-AAT-AAC-CAA-GT	
PDGF β	F	GCT-CTT-CCT-GTC-TCT-CTG-CTG	Eurofins
	R	AGA-TTG-GCT-TCT-TCC-GCA-CA	Genomics
RPSA	F	CCA-TTG-AAA-ACC-CTG-CTG-AT	Eurogentec
	R	CTG-CCT-GGA-TCT-GGT-TAG-TGA	
TIMP-2	F	GAG-CAC-CAC-CCA-GAA-GAA-GA	MWG
	R	GTG-ACC-CAG-TCC-ATC-CAG-AG	Biotech
TRAF6	F	TGC-CCT-ACA-GCC-CCA-ATTC	Eurofins
	R	GCA-TGC-ACA-GTT-TGT-ACC-CG	Genomics
TRPM7	F	AGT-TCC-AAG-GAC-CCT-C	Eurofins
	R	CCG-TTG-GGC-TCT-GTT-C	Genomics
uPA	F	CCC-AGT-TTG-GCA-CAA-GCT-GT	Eurogentec
	R	CCC-TGG-CAG-GAA-TCT-GTT-TTC	
VEGFA	F	CTC-ACC-AAG-GCC-AGC-ACA-TA	Eurofins
	R	TAA-CTC-AAG-CTG-CCT-CGCC	Genomics

Abbreviations: F, forward; MMP, matrix metalloproteinases; R, reverse; RBSA, ribosomal protein SA.

EVs mL^{-1}). Results were expressed as the cumulative cell number as a function of the time of culture, as previously described (Brassart et al., 2007).

2.10 | Cell migration and invasion assays

Migration and invasion were performed in modified Boyden chambers (8 μm pore) (Greiner bio-one). Before seeding the cells, Matrigel (10 μg per well, Corning) was added for invasion assay. 5×10^4 MIA PaCa-2 cells were seeded into the upper compartment

of the chamber, in 100 µL of DMEM medium containing 5% FBS. After 24 h, old medium was removed and 100 µL of DMEM with or without 10^9 PDAC-derived EVs or PDAC AG-9-derived EVs were added. The lower compartment was filled with only DMEM. After 48 h for the migration assay and 72 h for the invasion assay, inserts were washed with PBS and fixed with methanol for 20 min. Cells were stained with 0.1% crystal violet for 20 min. Cells that did not cross the membrane of the insert were removed mechanically using a cotton swab. Cells on the lower side of the membrane were then photographed using an inverted optical microscopy equipped with a camera (20× objective). The crystal violet coloration was eluted in 10% acetic acid for 10 min. The absorbance was measured using a SPECTROstar Nano microplate spectrophotometer (BMG Labtech) at 560 nm.

2.11 | Wound healing assay

HMEC-1 was allowed to grow to reach 90% of confluence in a 24-well plate in a complete medium at +37°C. The monolayers were scratched using individual 200 µL pipette tips. 10^9 PDAC-derived EVs or PDAC AG-9-derived EVs were added in a media containing 0.1% FBS. Images were acquired at different time using an inverted optical microscope equipped with a camera (20× objective). The wound area was quantified using ImageJ software (3 photographs per wound).

2.12 | Cell starvation and conditioned media collection

MIA PaCa-2 and HMEC-1 cells were seeded in 96-well plates (4.5×10^4 cells and 3×10^4 cells per well, respectively) in DMEM supplemented with 5% FBS. After 24 h, the medium was replaced by fresh FBS-free medium without EVs, with 10^9 PDAC-derived EVs or with 10^9 PDAC AG-9-derived EVs. Cells were incubated for 48 h and CM were harvested and centrifuged at 10,000 × g at +4°C for 10 min to remove cellular debris.

2.13 | Zymography analysis

The gels used are polyacrylamide gels supplemented with gelatin (1 mgmL^{-1}) to evidence pro-MMP-2 secretion (gelatin zymography), with MMP-2 (20 ng.mL^{-1} purified recombinant MMP-2) to detect TIMP-2 secretion (Brassart et al., 1998) (reverse zymography) and with plasminogen (3 µg mL^{-1}) to detect uPA secretion (gelatin/plasminogen zymography). The gels are cast with a 9% acrylamide separation gel (30% acrylogel, 1.5 M Tris, 10% SDS, TEMED, APS) and a 4% acrylamide concentration gel (30% acrylogel, 0.5 M Tris, 10% SDS, TEMED, APS). 10 µL of cell CM are mixed with the same volume of 2× loading buffer (10% SDS, 3% sucrose, 25 mM Tris, 0.02% bromophenol blue) and loaded on the gel. The migration is carried out at 10 mA by gel in a migration buffer (25 mM Tris, 192 mM glycine, 0.1% SDS (w/v), pH 8.3) for 90 min. After migration, the gels are incubated in a 2.5% (w/v) Triton X-100 solution for 2 × 30 min. The gels are then incubated separately in incubation buffer for 18 h at +37°C: 50 mM Tris, 5 mM $CaCl_2$, 0.02% (w/v) Triton X-100 pH 7.6 for gelatinolytic activity detection; 100 mM Glycine, 5 mM EDTA pH 8.3 for plasminogen activity. At the end of the incubation period, the gels are stained with a solution of Coomassie blue G-250 (0.5% [w/v] G250 Coomassie blue, 10% [v/v] glacial acetic acid, 40% [v/v] methanol) for 30 min with agitation and then destained in a bleaching solution (10% [v/v] methanol, 20% [v/v] acetic acid). Areas of enzyme activity appear as white bands against a dark blue background. The images of the gels are acquired using the Chemidoc device (Bio-Rad Laboratories), then the white bands are quantified using the ImageLab software (Bio-Rad Laboratories).

2.14 | Immunofluorescence cell staining

The MIA PaCa-2 and HMEC-1 cells were grown on glass coverslips (Electron Microscopy Services) in 24-well plates at a rate of 2×10^4 cells in 10% FBS-containing medium for 24 h. 10^9 PDAC-derived EVs or PDAC AG-9-derived EVs were added and incubated for 2 h at +4°C or 24 h at +37°C. Then, cells were fixed in a fixation buffer (4% paraformaldehyde [PFA] [Sigma-Aldrich] in PBS) for 15 min at RT. Cells were washed with PBS and permeabilized in a permeabilization buffer (0.1% Triton X-100 and 3% BSA in PBS) for 30 min at RT. Primary antibodies were incubated overnight at +4°C and Alexa Fluor 488 or Alexa Fluor 568-conjugated secondary antibodies for 60 min at RT in darkness in 0.1% Triton X-100 and 3% BSA in PBS. Negative controls were obtained with omission of the first antibody. Cells were washed and glass slides were mounted under a coverslip using the immune-mount Shandon (Thermo Fisher Scientific). Images were acquired using a Zeiss LSM 710 confocal laser scanner microscope (Carl Zeiss SAS) with the 63× oil-immersion objective (ON 1.4) coupled with CHAMELEON femtosecond Titanium-Sapphire Laser (Coherent, Santa, CA, USA). Alexa 488 was excited by the 488 nm line of Argon. Emitted signals were collected with a 493–560 nm bandpass filter. Alexa 568 was excited by the 561 nm line of Argon. Emitted signals were collected with

570–700 bandpass filters. Image acquisitions were processed and analysed using ZEN software (Carl Zeiss SAS). Mean cellular intensities of IF signal were quantified using ImageJ from 5 to 10 random fields at 63× magnification.

2.15 | Flow cytometry

2.15.1 | EV analysis with a bead-based multiplex

PDAC-derived EV and PDAC AG-9-derived EV samples were filtered with a 0.22 µm filter. Samples were subjected to bead-based multiplex analysis by flow cytometry (MACSPlex Exosome Kit, human, Miltenyi Biotec). This kit allows the detection of 37 exosomal surface epitopes plus two control isotypes. Samples were processed following the manufacturer's instructions and three detection antibodies were used separately. 0.5, 1 and 5×10^9 PDAC-derived EVs and PDAC AG-9-derived EVs were resuspended in PBS to a final volume of 120 and 10 µL of MACSPlex Exosome Capture Beads were added. Samples were incubated on an orbital shaker overnight at RT in darkness. Beads were washed in PBS and incubated for 1 h at RT with detection antibodies included in the kit (APC-conjugated anti-CD9, anti-CD63 and anti-CD81) were. PDAC-derived EVs and PDAC AG-9-derived EV samples were analysed in a BD LSRFortessa flow cytometer (Becton Dickinson Biosciences). The 39 individual bead populations were selected to allow determination of the APC signal intensity on the respective bead population and the median fluorescence intensity (MFI) for each capture bead was measured. MFI of each bead obtained from the control sample (PBS only) was subtracted from the signal intensities of the respective beads incubated with the sample. The mean of the MFI of the MACSPlex Exosome Capture Beads CD9, CD63 and CD81 was used as the normalisation factor for each sample. The data analysis was performed using the FlowLogic software (Inivai Technologies).

2.16 | PDAC-derived EVs uptake

MIA PaCa-2 cells were seeded (2×10^5 cells well^{-1}) in complete media in 24-well plates to reach 80% confluence the following day. The cells were incubated with 10^9 PDAC-derived EVs or PDAC AG-9-derived EVs at +37°C for 24 h. The cells were washed with PBS and detached with PBS containing 0.05% of trypsin/EDTA. After centrifugation, the cells were fixed in DPBS containing 4% PFA for 10 min at RT. After centrifugation ($300 \times g$ for 5 min) and washing, the cells were saturated with a PBS-Triton 0.1%-BSA 3% (PBS-T-BSA 3%) solution for 30 min at RT. After centrifugation and washing, primary antibodies were incubated for 1 h at RT. After centrifugation and washing, Alexa Fluor 488 or Alexa Fluor 568-conjugated secondary antibodies were incubated for 30 min in darkness in PBS-T-BSA 3% solution at RT. After centrifugation and washing, the cells were analysed in a BD LSRFortessa flow cytometer and data analysis with FlowLogic software.

2.17 | Pseudotube formation assay

The capillary tube structures of HMEC-1 were evaluated on precoated Matrigel (Corning). Matrigel (200 µL per well of a 11.8 mg mL^{-1} solution) was allowed to polymerize for 30 min at +37°C. HMEC-1 cells were seeded (5×10^4 cells well^{-1}) in 48-well plate precoated by Matrigel in DMEM free FBS with or without 10^9 PDAC-derived EVs or PDAC AG-9-derived EVs. Pseudotube formation was allowed to proceed for as long as 24 h at +37°C. Cells were fixed for 30 min with glutaraldehyde 1.1% (Sigma Aldrich) and pictures were taken using an inverted optical microscope equipped with a camera (10× objective). The number of isolated segments, segments, junctions, mesh area and nodes were measured with ImageJ software via Angiogenesis Analyser plugin (mean ± standard error of mean [SEM]).

2.18 | Scanning electron microscopy

The MIA PaCa-2 and HMEC-1 cells were grown on glass coverslips (Electron Microscopy Services) in 24-well plates at a rate of 2×10^4 cells in 10% FBS-containing medium for 24 h. Cells were rinsed twice with PBS (Gibco) and then fixed with 2.5% glutaraldehyde in PBS (Sigma Aldrich) for 1 h at RT. After gradual dehydration in ethanol (in % 50, 70, 90 and 100 twice), the samples were immersed in hexamethyldizilazane (Sigma Aldrich) for 5 min, air dried at RT and finally sputtered with a thin gold–palladium film under a JEOL ion sputter JFC 1100. Cells were visualized using a LaB6 electron microscope (JEOL JSM-5400 LV, JEOL) at an acceleration voltage of 20 kV using the secondary electron signal.

2.19 | Correlative light and electron microscopy

The MIA PaCa-2 and HMEC-1 cells were grown on 22 mm square glass in culture dishes to 25% confluence. Cells were stained with 4 μM calcein red (Thermo Fisher Scientific) for 30 min in cell culture media FBS-free. After 2 h treatment with PDAC-derived EVs (10^9 mL^{-1}), cells were fixed in a fixation buffer solution (4% PFA in PBS) for 15 min at RT. Cells were washed with PBS and permeabilized in a permeabilization solution PBS-T-BSA 3% for 30 min at RT. Primary antibodies (anti-GFP and anti-FLuc) were incubated overnight at +4°C and Alexa Fluor 405 or Alexa Fluor 488-conjugated secondary antibodies for 90 min at RT in darkness in PBS-T-BSA 3% 0.1%. After washing, cells were fixed in a 2.5% glutaraldehyde (Sigma Aldrich) in PBS solution. After washing in PBS and milliQ water, samples were dehydrated in gradual concentration of ethanol (in % 25, 50, 75, 90 and 100 twice) solutions, 50% of 100% ethanol and 50% of hexamethyldisilazane (Sigma Aldrich) solution, immersed with hexamethyldisilazane and were air dried using the critical point drying method. Finally, samples were sputtered with a thin gold–palladium film under a SCIENTEC SPT 20 (Scientec). The cells were observed with the EVO10 SEM (Carl Zeiss SAS) equipped with correlative support for square glass cover slip. Confocal acquisition from LSM 880 (Carl Zeiss SAS) were produced images using ZEN software (Carl Zeiss SAS). Saved positions of cells were correlated with ZEN Connect module between confocal and SEM and dedicated and fluorescence images were fitted to the electron micrographs using the ZEN program.

2.20 | Immunogold labelling of EVs and transmission electron microscopy

For transmission electron microscopy, freshly isolated EVs suspensions were fixed in 4% PFA for 1 h. PDAC-derived EV samples (approximately 5 μL) were applied to copper mesh Formvar coated carbon stabilised grids, were allowed to adsorb to the grid for 5 min and then were wicked off with filter paper. For negative staining of exosomes, UA-Zero EM stain (Agar Scientific) was applied to the grid for 90 s, then wicked off with Whatman filter paper. Grids were allowed to thoroughly dry before viewing.

As for immunoelectron labelling with anti-CD63, anti-RPSA and anti-Fluc, exosome samples were fixed overnight in 4% PFA diluted in 0.1 M cacodylate buffer (pH 7.4). Fixed EV preparations (20 μL) were applied to a carbon-Formvar coated 200 mesh nickel grids, and samples were allowed to stand for 30 min before wiping off excess using Whatman filter paper. Grids were then floated (sample side down) onto a 20 μL drop of 1 M ammonium chloride for 30 min to quench aldehyde groups from the fixation step, followed by floating on drops of blocking buffer (0.4% BSA in PBS) for 2 h. Grids were rinsed 3 times (5 min each) using PBS and then incubated with either blocking buffer only (negative control) or primary antibody (CD63, RPSA, eGFP or FLuc) diluted with blocking buffer (1:100) for 18 h. Rinsing of the grids using deionized water (3 times for 5 min each) and PBS followed the incubation step. Grids were then floated on drops of 10 nm antirabbit nanogold and 10 nm antimouse nanogold (Abcam) diluted 1:50 in blocking buffer for 1 h. As a final step, negative staining in UA-Zero EM stain was performed, and samples were wicked dry and then allowed to air dry. Isolated EVs were visualised at room temperature using a FEG electron microscope (JEOL-JEM-2100F, JEOL) fitted with a CCD camera (Orius SC200D, Gatan) at an accelerating voltage of 200 kV.

2.21 | In vivo experiments

In vivo experiments in mice were conducted according to the European Directive 2010/63/EU on the protection of animals used for scientific purposes and the respective Belgian (Royal Decree of 29 May 2013) and Flemish regulations (Decision of the Flemish Government to adapt the Royal Decree of 29 May 2013, 17 February 2017) for principles of laboratory animal care. The in vivo experimental procedures were approved by the Animal Ethics Committee of KU Leuven (ECD p259/2015). Based on previous data obtained in the in vivo PDAC model (Nannan et al., 2023), the power calculation for the application of the ECD was performed resulting in sample size of $n = 3$ to demonstrate a significant effect of EDPs. Six week old female Swiss Nude *nu/nu* (Nu(Ico)-*Foxn1^{nu}*) mice (average body weight, 20–24 g) were purchased from Charles River Laboratories. Animals were housed at the animal facility of KU Leuven using standard, individually ventilated cages under a 12 h light/dark schedule in controlled environmental conditions of humidity (50%–70%) and temperature (+22 ± 2°C) with food and water supplied *ad libitum*. All mice were acclimatized to our laboratory conditions for 1 week before starting the experiments. For induction of the tumour model and imaging, mice were anesthetized using 2% isoflurane (IsoVET, 100 mg g^{-1}, Eurovet, Piramal, Healthcare) in 100% O$_2$. Mice were sacrificed at the end of the experiments.

2.22 | Subcutaneous xenograft model

For the subcutaneous (s.c.) PDAC model, 5×10^6 MIA PaCa-2 cells in suspension in 100 μL of sterile PBS were implanted subcutaneously into the right lower flank regions. Tumours were allowed to grow for 4 weeks. Animals were randomized in four different groups: control, NaCl, PDAC-derived EVs and PDAC AG-9-derived EVs ($n = 3$ per group).

2.23 | Bioluminescence imaging

In vitro and in vivo BLI was performed using an IVIS Spectrum imaging system (Perkin Elmer). BLI was performed to reflect intensity of FLuc from PDAC-derived EVs. For in vitro experiment, PDAC-derived EVs were added on a 96-well plate (Nunclon Delta-surface, Thermo Fisher Scientific) before imaging. An equal volume of D-luciferin solution (final concentration 0.2 µg mL^{-1}, Luciferin-EF, Promega) was added and a well containing PBS and D-luciferin was used as a control. The signal intensity (normalised photon flux in p per s cm^{-2} per sr]) was correlated with the number of PDAC-derived EVs present in each well. Regions of interest (ROIs) were placed over each well for quantification of the total photon flux using Living Image, version 4.2 (Perkin Elmer). The BLI signal was acquired using the following settings: exposure time of 5 min per image, F/Stop of 1, a subject height of 1.5 cm, field-of-view of 22.8 cm and medium binning. For in vivo experiments, animals ($n = 3$ per group) were anesthetized using 2% isoflurane (IsoVET, 100 mg g^{-1}, Eurovet, Piramal, Healthcare) in 100% O$_2$ (2 L min^{-1}). PDAC-derived EVs and PDAC AG-9-derived EVs were resuspended extemporaneously with sterile PBS (Gibco) and an equal volume of D-luciferin solution (final concentration 0.2 µg mL^{-1}, Luciferin-EF) to reach a final concentration of 3.5×10^{11} kg^{-1} (mouse weight) for the intravenous injection (i.v.). I.v. administrations of PDAC-derived EVs or PDAC AG-9-derived EVs were performed at zero time point. A second dose of D-luciferin was injected after 30 min. Upon completion of BLI detection, the total photon flux (p s^{-1}) was quantified over various body regions like body (ROI of 20.3 cm^2), head (ROI of 7.5 cm^2), thorax (ROI of 6 cm^2), abdomen (ROI of 7.5 cm^2) and tumour (ROI of 1.9 cm^2) as a function of incubation time after EV injection.

2.24 | Statistical analysis

GraphPad Prism 8.2 software (GraphPad) was used for all statistical analysis. Data are expressed as the mean $\pm$ SEM, SD or Min to Max. Mann–Whitney U test and Student's t test was used for in vitro experiments. For all tests, statistical significance was assumed when $p < 0.05$ (*), $p < 0.01$ (**, \$\$), $p < 0.001$ (***) and $p \leq 0.0001$ (****). * when we compared control to EVs and \$ when we compared PDAC-derived EVs to PDAC AG-9-derived EVs. For in vivo experiment, *2-way ANOVA* test was used and data are expressed as the mean $\pm$ SD. Statistical significance was assumed when, $p < 0.05$ (*), $p < 0.01$ (**), $p < 0.001$ (***), $p \leq 0.0001$ (****), when we compared group 1 to other groups, $p < 0.05$ (#), $p < 0.01$ (##), $p \leq 0.0001$ (####), when we compared group 2 to groups 3 and 4 and $p < 0.05$ (\$), $p < 0.01$ (\$\$), when we compared group 3 to group 4).

3 | RESULTS

3.1 | Characterisation of PDAC-derived EVs and PDAC AG-9-derived EVs

To investigate the influence of the microenvironment on PDAC EV fate and activities in vitro and in vivo, MIA PaCa-2 cells were transduced to express two markers, eGFP and FLuc (PDAC cells [MIA PaCa-2/eGFP-FLuc$^+$]) (Figure S1) (Nannan et al., 2023). After AG-9 treatment [10^{-7} M] for 24 h, isolated EVs were characterised. TEM analysis demonstrated the presence of EVs in PDAC cell culture media (Figure 1a). Isolated EVs showed different NTA profiles (Figure 1b). As previously shown for fibrosarcoma HT-1080 cells (Brassart et al., 2019), AG-9 treatment affects the average size of EVs. While PDAC-derived EVs presented a mean diameter of 144.2 $\pm$ 2.0 nm, PDAC AG-9-derived EVs had a mean diameter of 164.2 $\pm$ 8.3 nm (Figure 1b). The presence of AG-9 in PDAC cell culture media significatively stimulate EVs secretion by almost 2-fold (PDAC-derived EVs: $1.50 \times 10^8 \pm 0.28 \times 10^8$ EVs mL^{-1}; PDAC AG-9-derived EVs: $2.92 \times 10^8 \pm 1.04 \times 10^8$ EVs mL^{-1}; $p \leq 0.0001$ [****]) (Figure 1c). Protein content analysis of isolated EVs by WB (Figure 1d), anti-CD63 TEM-immunogold labelling (Figure 1e) and flow cytometry (multiplex assay) (Figure 1f) confirmed the presence of CD9, CD63, CD81 markers and the absence GM130 apoptotic marker. mRNA- and protein-level content analysis of EVs by RT-qPCR (Figure 1 g), WB (Figure 1h) and TEM-immunogold labelling (Figure 1i), revealed the presence of eGFP and FLuc. As AG-9 modulates many cellular activities through RPSA, we wanted to define whether EVs could carry this receptor in order to transmit it to EV-receiving cells. As shown in Figure 1j–l, EVs contain both RPSA mRNA and protein as well as the transcript and TRPM7 protein (Figure S2), the complex TRPM7/RPSA being known to regulate human PDAC cell migration (Lefebvre et al., 2020).

3.2 | PDAC-derived EVs and PDAC AG-9-derived EVs differentially stimulate PDAC proliferation

As AG-9 modulated EV size and concentration, we decided to study the impact of the isolated EVs on PDAC cell proliferation. EVs were resuspended in equal volumes of medium (1.5×10^8 PDAC-derived EVs per millilitre or 3×10^8 PDAC AG-9-derived EVs per millilitre) and added on PDAC cell. As shown in Figure 2, after 4 days of treatment with PDAC-derived EVs or AG-9-
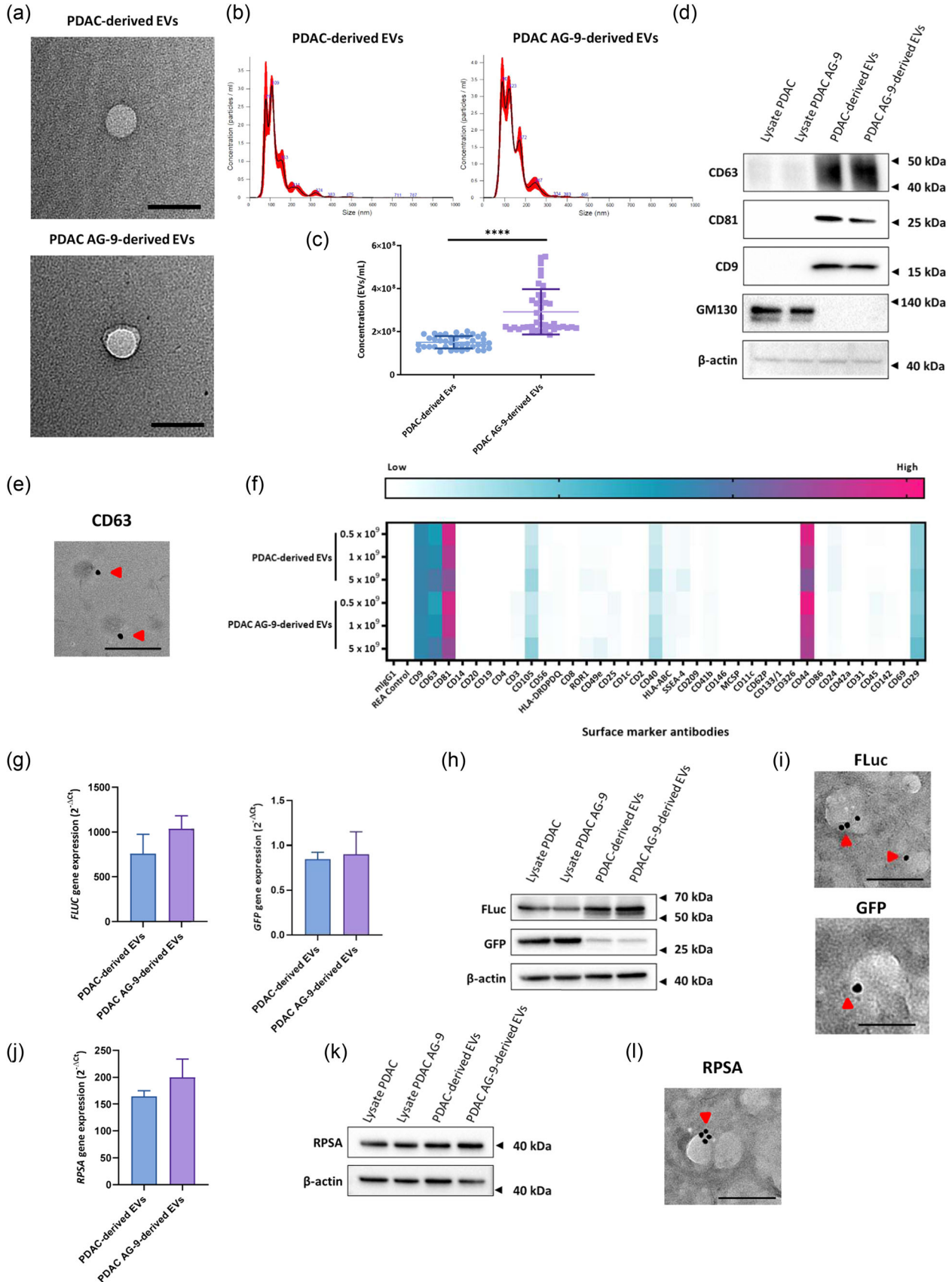
FIGURE 1 Characterisation of PDAC-derived EVs and PDAC AG-9-derived EVs. (a) TEM images of isolated EVs. Scale bar: 100 nm. (b) Graphs showing particle number and size distribution of EVs using NTA. (c) EV concentration determined by NTA (scatter dot plot, mean ± SD; $N = 8$, $n = 4$; ****, $p \leq 0.0001$; Student's t test). (d) WB on total protein of cell extracts and their EVs with CD63, CD81, CD9 and GM130 EV markers. β-Actin was used as an internal control ($N = 3$). (e) TEM-immunogold labelling image of isolated EVs using anti-CD63 antibody. Red arrows show gold particles (10 nm). Scale bar: 100 nm. (f)
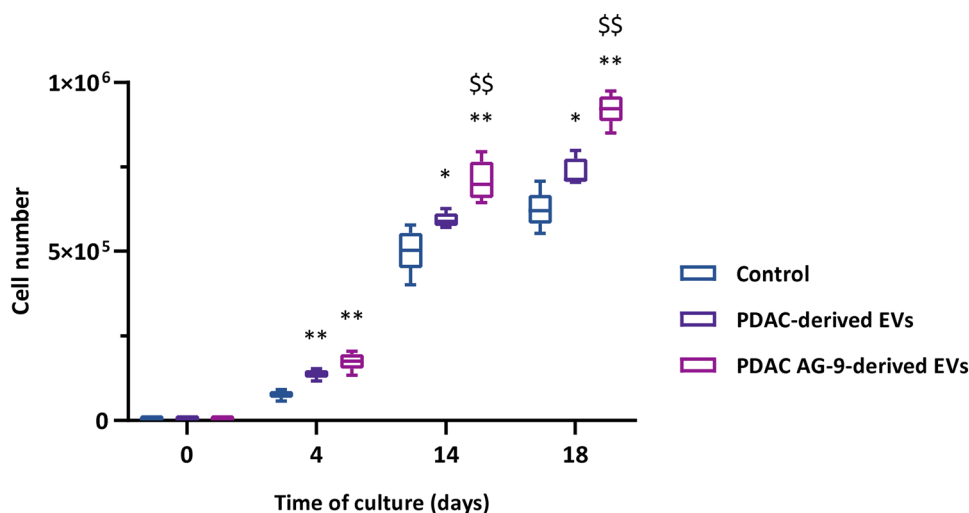
(Continues)

FIGURE 2 Proliferation curves for long-term cultures of PDAC cell line treated with PDAC-derived EVs (1.5×10^8 EVs/mL) and PDAC AG-9-derived EVs (3×10^8 EVs mL^{-1}). The proliferation is expressed in population doublings as a function of days of culture (Box and whiskers; Min to Max.; $n = 5$; *, $p < 0.05$, **, $p < 0.01$, when we compared control to EVs and $$, $p < 0.01$, when we compared PDAC-derived EVs to PDAC AG-9-derived EVs; *Mann-Whitney U* test). EV, extracellular vesicles; PDAC, pancreatic ductal adenocarcinoma.

derived EVs per millilitre, PDAC cell proliferation was significantly increased by 1.78 ± 0.15-fold and 2.26 ± 0.30-fold, respectively ($p < 0.01$ [**]) compared to untreated cells. In long-term cell growth studies, PDAC AG-9-derived EVs significantly stimulate EV recipient cell proliferation compared to PDAC-derived EVs (1.19-fold, $p < 0.01$ [$$]). Proliferation of PDAC cells treated with 1.5×10^8 PDAC-derived EVs per millilitre or 3×10^8 PDAC AG-9-derived EVs per millilitre was increased by 0.98 ± 0.14-fold ($p < 0.05$ [*]) and 1.57 ± 0.15-fold ($p < 0.01$ [**]) respectively after 14 days of incubation and 1.01 ± 0.08 ($p < 0.05$ [*] and 1.48 ± 0.07 ($p < 0.01$ [**]) respectively after 18 days of incubation. This experiment showed that AG-9, a peptide released in tumour microenvironment, is able to modulate the release of EVs and, by the way, tumour cell proliferation.

3.3 | In vitro cellular uptake of PDAC-derived EVs and PDAC AG-9-derived EVs by PDAC cancer cells

The previous experiment on cell proliferation and its outcome were parameterized on the finding of a deregulation of EVs release under the influence of the microenvironment illustrated by the addition of AG-9 in the culture medium. To normalise and standardise the rest of the study, the addition of EVs in each of the following experiments was controlled and defined at 10 (Betre et al., 2006) EVs per millilitre in each experimental condition.

The biological activities induced by EVs on recipient cells can be conditioned by modulations of EV integration. After 1 h of incubation in the presence of 10^9 PDAC-derived EVs or PDAC AG-9-derived EVs per millilitre, surface of recipient PDAC cell was studied by scanning electron microscopy (SEM) showing presence of EVs (Figure 3a). To prove that the EVs present at the cell surface were exogenous EVs, isolated from PDAC eGFP-FLuc cells, and not EVs resulting from recipient cell biogenesis, correlative microscopy was performed using anti-GFP and anti-FLuc antibodies. After addition of EVs and incubation for 1 h at $+37°C$, PDAC recipient cells exhibited eGFP-FLuc$^+$ EVs at their plasma membrane (Figure 3b). Immunofluorescence staining with anti-GFP and anti-FLuc on PDAC cells after adding 10^9 EVs in culture media for 2 h showed eGFP and FLuc presence in all recipient cell bodies (Figure 3c). However, quantification of eGFP and FLuc signals in recipient PDAC cells showed no significant difference between both EV treatments (Figure 3d). Although AG-9 modulates the release of EVs by tumour cells, it
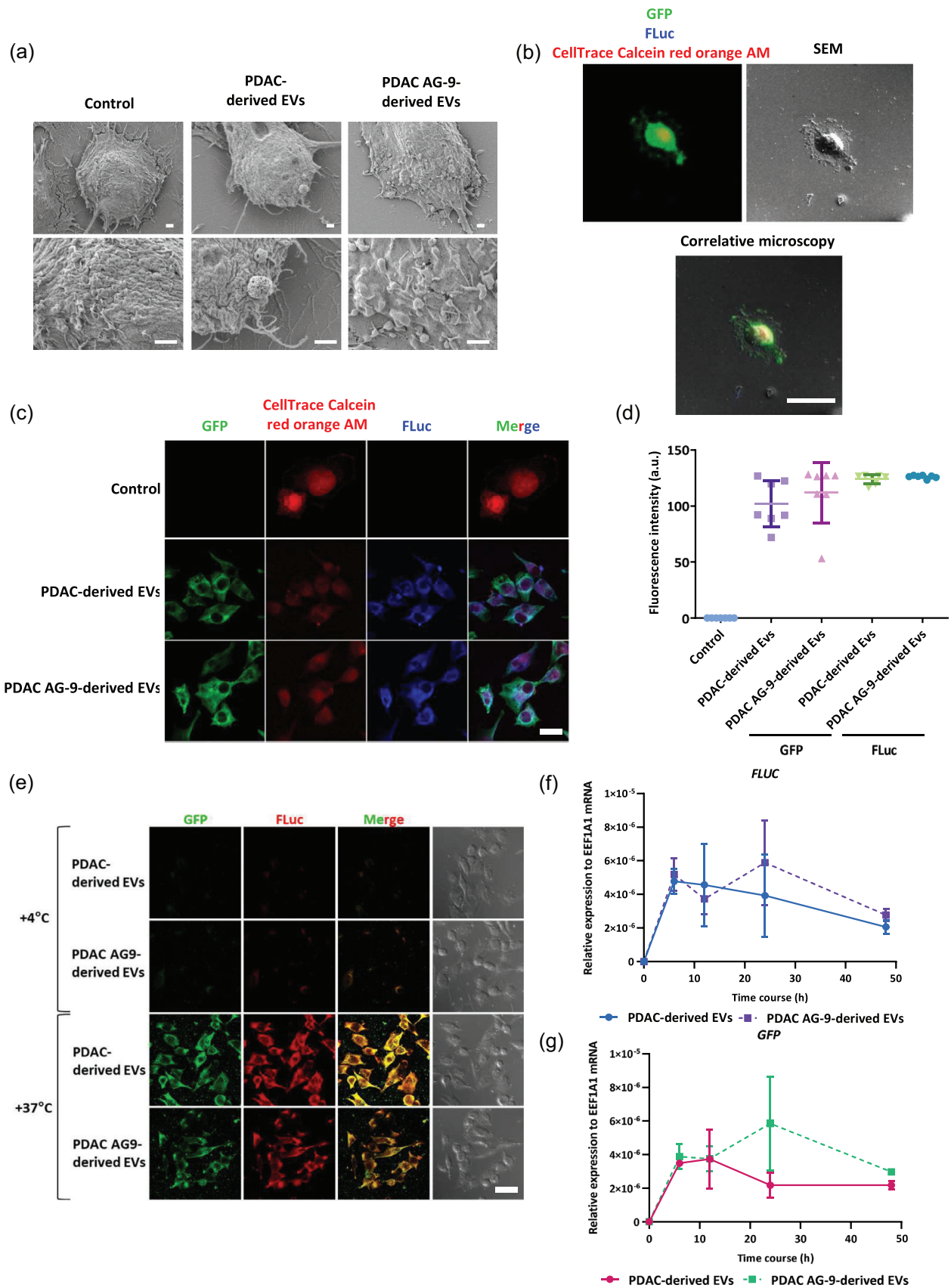
FIGURE 3 In vitro cellular uptake of PDAC-derived EVs and PDAC AG-9-derived EVs by PDAC cancer cells. (a) Autologous PDAC cellular uptake of EVs (10^9 EVs mL^{-1}) by PDAC cells after 1 h of incubation analysed by SEM ($N = 2$, $n = 2$). Scale bar: 1 μm. (b) Correlative microscopy on PDAC cells. Immunofluorescence staining on PDAC cells (4 μM calcein red) for eGFP (anti-GFP; green) and FLuc (anti-FLuc; blue) after EV treatment (10^9 EVs mL^{-1}), optical z-stack and SEM scanning ($n = 5$). Scale bar 10 μm. (c) Immunofluorescence staining on PDAC cells for eGFP and FLuc after EVs (10^9 EVs mL^{-1}) cell

(Continues)

does not seem to influence EV uptake by recipient cancer cells. By incubating the recipient PDAC cells with 10^9 EVs per millilitre at +4°C, the membrane dynamics of the cell is blocked excluding EV endocytosis phenomena. Under these conditions, the uptake of EVs is strongly reduced. At +37°C, all cell bodies show the markers eGFP and FLuc (Figure 3e). The kinetics of EV uptake (10^9 EVs mL^{-1}) on recipient PDAC cells by tracking eGFP and FLuc marker transcripts was studied using RT-qPCR. The gene expression of eGFP and FLuc markers occurs as soon as 6 h after incubation for both conditions. The maximum for eGFP and FLuc was obtained for the 24 h time with the PDAC AG-9-derived EV conditions with ratios of $5.89 \times 10^{-6} \pm 2.46 \times 10^{-6}$ and $5.91 \times 10^{-6} \pm 2.92 \times 10^{-6}$, respectively (Figure 3f,g) and was still detectable after 48 h. Treatment of recipient cells with cycloheximide (20 µM) did not induce any change in the protein expression of these markers after 24 h of incubation (Figure S3a,b). The protein transfer of eGFP and FLuc to recipient cells was sufficient to confer the eGFP-FLuc$^+$ phenotype (Figure S3c,d).

3.4 | In vitro cellular uptake of PDAC-derived EVs and PDAC AG-9-derived EVs by endothelial cells

We previously demonstrated that AG-9 stimulates in vitro and in vivo angiogenesis (Da Silva et al., 2018, Nannan et al., 2023). We studied the uptake of tumour EVs by endothelial HMEC-1 cells. After 1 h of incubation in the presence of 10^9 EVs mL^{-1}, recipient HMEC-1 cell surface studied by SEM showed EV presence (Figure 4a). As for PDAC cells, incubation of HMEC-1 cells for 1 h at +37°C with EVs allowed visualisation of eGFP-FLuc$^+$ EV adhesion on the plasma membrane of recipient cells, by correlative microscopy (Figure 4b). A longer incubation allows to see the dispersion of the EV content (eGFP and FLuc) in the whole cell body (Figure 4c). Quantification of eGFP and FLuc signals in recipient HMEC-1 cells showed no significant difference between PDAC-derived EVs and PDAC derived-AG-9 EVs (Figure 4d). If the AG-9 peptide from the microenvironment modulates EV release by cancer cells, it does not seem to modify EV uptake by endothelial recipient cells. The uptake is significantly decreased when recipient cells are incubated at +4°C (Figure 4e), meaning that the transfer of eGFP and FLuc is an active process and not a passive one. The kinetics of tumour EV uptake by recipient HMEC-1 cells by tracking eGFP and FLuc marker transcripts was studied using RT-qPCR (Figure 4f–g). The detection kinetics of both markers in HMEC-1 cells was similar to that in PDAC cells. Detectable as early as 6 h postincubation, eGFP and FLuc transcripts were still detectable in HMEC-1 recipient cells after 48 h of incubation. The maximum ratio for eGFP was obtained at 24 h in the PDAC AG-9-derived EV condition ($4.62 \times 10^{-5} \pm 1.93 \times 10^{-5}$). By contrast, the maximum ratio for FLuc was obtained at 6–12 h in the control condition ($3.79 \times 10^{-5} \pm 1.05 \times 10^{-5}$). Treatment of HMEC-1 recipient cells with cycloheximide (20 µM) did not induce any change in the protein expression of these markers after 24 h of incubation (Figure S4a-b). The protein component contained in EVs appears to be sufficient to allow HMEC-1 cells to transform into HMEC-1/eGFP-FLuc$^+$ cells.

3.5 | In vitro effect of PDAC-derived EVs and PDAC AG-9-derived EVs on PDAC cell proliferation, migration and invasion

The incubation of PDAC cells in the presence of EVs released under AG-9 peptide treatment or control condition stimulated PDAC cell proliferation (Figure 2). This effect could be dependent on the different EV amount added in the conditioned media. Proliferation studies were performed under standardised conditions. The same concentration of EVs (10^9 EVs mL^{-1}) was added to PDAC cell culture media and incubated for 72 h. EV treatments significantly induced proliferation: 1.31-fold increase for PDAC-derived EVs ($p < 0.001$ [***]) and 1.40-fold increase for PDAC AG-9-derived EVs ($p < 0.001$ [***]) (Figure 5a). Incubation with EVs significantly increased the migration of PDAC cells with a 1.31-fold increase for PDAC-derived EVs ($p < 0.05$ [*]) and 1.40-fold increase for PDAC AG-9-derived EVs ($p \leq 0.0001$ [****]) (Figure 5b). However, there were no significant differences in PDAC cell invasion (Figure 5c).
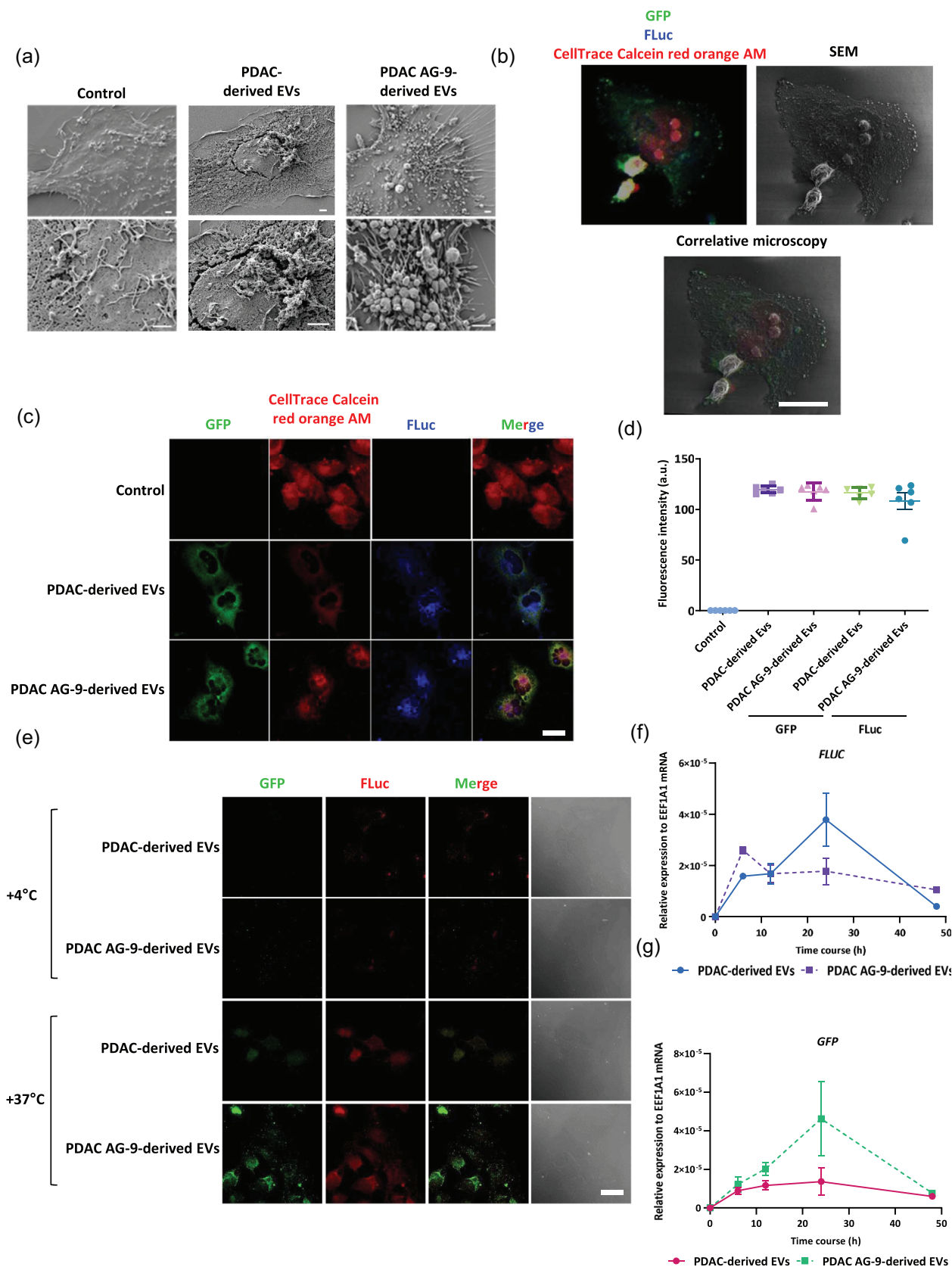
FIGURE 4 In vitro cellular uptake of PDAC-derived EVs and PDAC AG-9-derived EVs by endothelial cells. (a) Paracrine PDAC cellular uptake of EVs (10^9 EVs mL^{-1}) by HMEC-1 cells after 1 h of incubation analysed by SEM ($N = 2$, $n = 2$). Scale bar: 1 µm. (b) Correlative microscopy on HMEC-1. Immunofluorescence staining on HMEC-1 (4 µM calcein red) for eGFP (anti-GFP; green) and FLuc (anti-FLuc; blue) after EV treatment (10^9 EVs mL^{-1}), optical z-stack and SEM scanning ($n = 5$). Scale bar 20 µm. (c) Immunofluorescence staining on HMEC-1 cells for eGFP and FLuc after EV (10^9 EVs mL^{-1}) cell

(Continues)

FIGURE 4 (Continued)

incubation for 2 h and z-stack scanning. HMEC-1 cells were labelled with calcein red (4 μM calcein red) ($N = 2$, $n = 2$). Scale bar: 20 μm. (d) Quantification of anti-GFP and anti-FLuc signals on HMEC-1 cells after EV uptake (scatter dot plots; mean ± SD; $N = 3$, $n = 7$). (e) Immunofluorescence staining on HMEC-1 cells for eGFP and FLuc after EV (10^9 EVs mL^{-1}) cell incubation at +4°C and +37°C for 2 h and z-stack scanning. Scale bar: 40 μm. (f–g) Quantitative RT-PCR analysis of *FLUC* and *eGFP* mRNA at different time points after treatment of HMEC-1 cells with EVs (10^9 EVs mL^{-1}). *eEF1a1* was used as an internal standard (mean ± SEM; $N = 2$, $n = 3$). EV, extracellular vesicles; PDAC, pancreatic ductal adenocarcinoma.
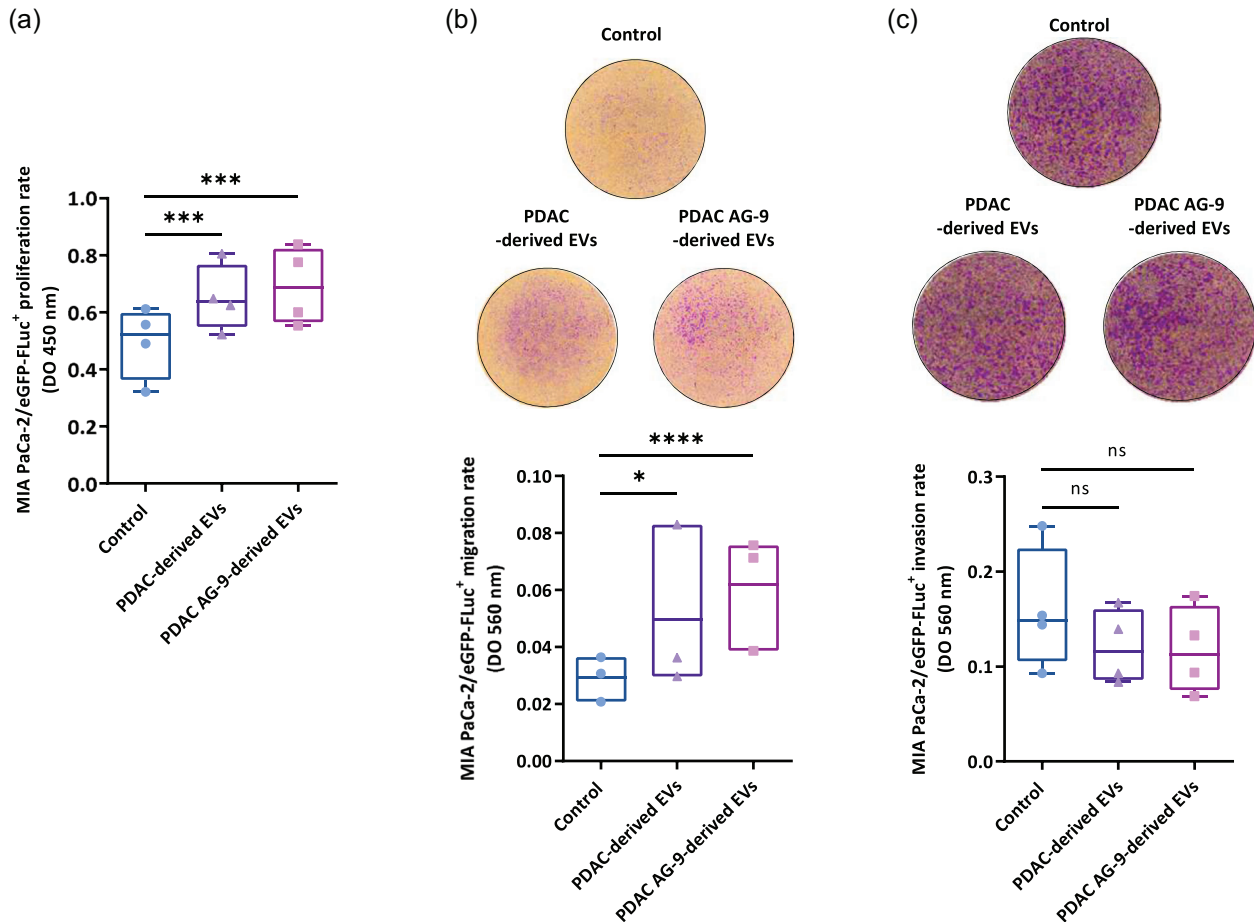

FIGURE 5 In vitro effect of PDAC-derived EVs and PDAC AG-9-derived EVs on PDAC progression. (a) Proliferation of PDAC cells after treatment with EVs (10^9 EVs mL^{-1}). Cell proliferation rate measurement by WST-1 assay at 72 h (box and whiskers; Min to Max.; $N = 4$, $n = 3$; ***, $p < 0.001$; Student's t test). (b) Migration of PDAC cells after treatment with EVs (10^9 EVs mL^{-1}). Cell migration evaluation by transwell assay system at 48 h (box and whiskers; Min to Max.; $N = 3$, $n = 3$; *, $p < 0.05$, ****, $p \leq 0.0001$; Student's t test). (c) Invasion of PDAC cells after treatment with EVs (10^9 EVs mL^{-1}). Cell invasion determination by transwell assay system coated with Matrigel at 72 h (box and whiskers; Min to Max.; $N = 4$, $n = 3$; ns, not significant; Student's t test). EV, extracellular vesicles; PDAC, pancreatic ductal adenocarcinoma.

3.6 | In vitro effect of PDAC-derived EVs and PDAC AG-9-derived EVs on PDAC cell proteinase and receptor expression

PDAC cells were cultured in the presence of 10^9 EVs for 48 h. FBS-free conditioned media were collected and analysed by gelatin zymography. In the absence of EVs, PDAC cells secreted a basal level of Pro-MMP-2 (Figure 6a). A 48 h treatment of PDAC cells with 10^9 EVs resulted in an increase in Pro-MMP-2 release, with a maximum of 1.77-fold reached for PDAC AG-9-derived EVs (1.61-fold for PDAC-derived EVs) (Figure 6a). EVs had no effect on the Pro-MMP-2 activation as no active MMP-2 form was detected in culture media. EVs had no significant effect on uPA secretion by PDAC cells, as demonstrated by plasminogen zymography (Figure 6b). TIMP-2 secretion in culture media was analysed by reverse zymography (Figure 6c). While treatment with PDAC AG-9-derived EVs tended to decrease TIMP-2 secretion by PDAC cells, PDAC-derived EVs significantly inhibited TIMP-2 secretion by 0.80-fold ($p < 0.05$ [*]) compared to control conditions.

Cell surface receptor expression, like integrins and RPSA elastin receptor expression, was analysed at protein and mRNA levels by WB and RT-qPCR, respectively. By WB study, compared to actin, β1 integrin subunit (ITGβ1) expression was inhibited in EVs
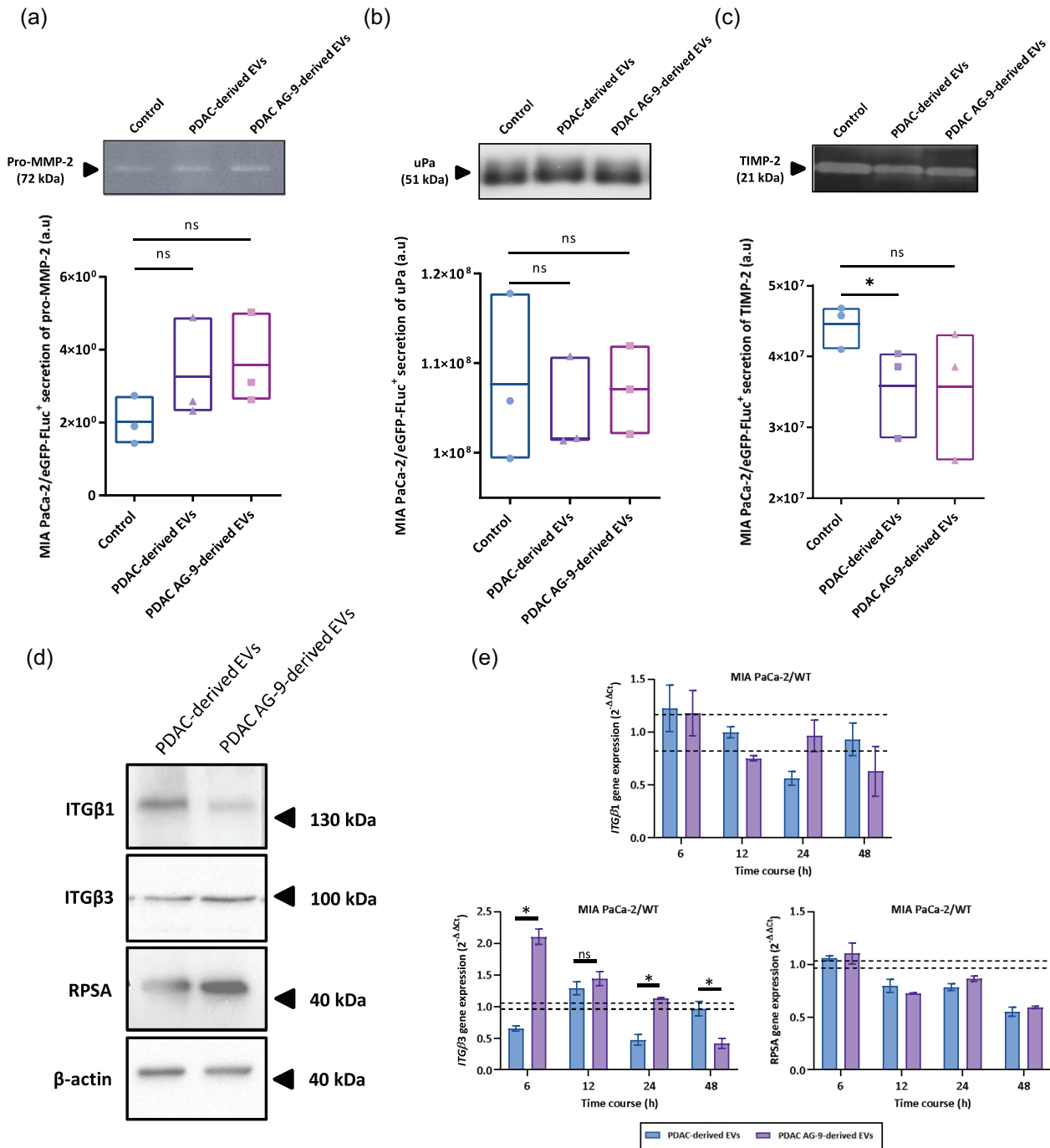
FIGURE 6 In vitro effect of PDAC-derived EVs and PDAC AG-9-derived EVs on PDAC cell proteinase and receptor expression. (a) Pro-MMP-2 secretion by PDAC cells after treatment with EVs (10^9 EVs mL^{-1}). Pro-MMP-2 secretion measurement by gelatin zymography after 48 h of incubation (box and whiskers; Min to Max.; $N = 3$, $n = 4$; *ns*, not significant; *Mann-Whitney U* test). (b) uPA secretion by PDAC cells after treatment with EVs (10^9 EVs mL^{-1}). uPA secretion measurement by gelatin/plasminogen zymography after 48 h of incubation (box and whiskers; Min to Max.; $N = 3$, $n = 4$; *ns*; *Mann-Whitney U* test). (c) TIMP-2 secretion by PDAC cells after treatment with EVs (10^9 EVs mL^{-1}). TIMP-2 secretion measurement by reverse zymography after 48 h of incubation (box and whiskers; Min to Max.; $N = 3$, $n = 4$; *, $p < 0.05$, *ns; Mann-Whitney U* test). (d) Integrin and RPSA expression by PDAC cells after treatment with EVs (10^9 EVs/mL). β1 (ITGβ1) and β3 (ITGβ3) subunit integrins and RPSA receptor expression measurement by WB after 24 h incubation. β-actin was used as an internal control ($n = 3$). (e) Quantitative RT-PCR analysis of *ITGβ1*, *ITGβ3* and *RPSA* mRNA at different time points after treatment of PDAC cells with EVs (10^9 EVs mL^{-1}). *eEF1a1* was used as an internal standard (the minimum and maximum SEM from control condition [time course of 0 h] are shown on the graphs by dashed lines; mean ± SEM; $N = 2$, $n = 3$) (*, $p < 0.05$; *Mann-Whitney U* test). EV, extracellular vesicles; PDAC, pancreatic ductal adenocarcinoma.

(Figure 6d). By contrast, β3 integrin subunit (ITGβ3) and RPSA receptor expressions were stimulated with PDAC AG-9-derived EV compared to PDAC-derived EV (Figure 6d). If the content of mRNA (ITGαv, ITGα5, ITGβ1, uPA, TIMP2 and MMP14 mRNA) in vesicles is identical in the different experimental conditions (control and AG-9) (**Figure S5**), ITGβ1, ITGβ3 and RPSA elastin receptor gene expression by PDAC cells were studied using RT-qPCR (Figure 6e). ITGβ1 and RPSA elastin receptor transcripts were not significantly modified. An 3.21-fold ($p < 0.05$ [*]) increase of ITGβ3 transcript was observed after 6 h and a 2.39-fold ($p < 0.05$ [*]) increase was observed after 24 h of treatment with PDAC-AG-9 derived EVs compared to PDAC-derived EVs. Microenvironment derived-peptides, such as AG-9, may modulate cellular receptor expression through EVs.

3.7 | Effect of PDAC-derived EVs and PDAC AG-9-derived EVs on HMEC-1 proliferation, migration and proteinase expression

HMEC-1 cells were cultured in the presence of 2.5% FBS supplemented with 10^9 EVs for 72 h. Compared to control cells, treatment with 10^9 EVs induced an increase in HMEC-1 proliferation: an 1.24-fold increase with PDAC-derived EVs ($p < 0.01$ [**]) and 1.22-fold increase with PDAC AG-9-derived EVs ($p < 0.01$ [**]) (Figure 7a). A scratch assay was performed to study the migration of HMEC-1 cells under the influence of EVs. It was conducted in the absence of FBS to avoid cell proliferation. No significant modification was observed between the different treatments after 24 and 48 h of incubation (Figure 7b).

MMP-14 expression was analysed by western blot on HMEC-1 cell extracts. Conditioned media were collected and analysed by zymography. HMEC-1 cells cultured for 48 h in the absence of EVs expressed a basal level of MMP-14, pro- and active forms (Figure 7c). A 48 h treatment of HMEC-1 cells with 10^9 EVs caused an increase in MMP-14 protein (pro-, active and auto-processed forms). Namely, the autoprocessed form is shown to be related to the activation process of pro-MMP-2 to MMP-2 via the formation of a pro-MMP-2/TIMP-2/MMP-14 complex. A 48 h treatment of HMEC-1 with 10^9 EVs from caused a significant increase in Pro-MMP-2 release: 1.64-fold increase with PDAC-derived EVs ($p \leq 0.0001$ [****]) and 1.57-fold increase with PDAC AG-9-derived EVs ($p \leq 0.0001$ [****]) (Figure 7d). No active MMP-2 form was detected in culture media analysed by gelatin zymography. In contrast to PDAC cells, EVs significantly stimulated uPA secretion, analysed by plasminogen zymography: 1.94-fold increase with PDAC-derived EVs ($p \leq 0.0001$ [****]) and 2.13-fold increase with PDAC AG-9-derived EVs ($p < 0.001$ [***]) (Figure 7e). EVs had no significant effect on the production of TIMP-2 by HMEC-1 cells analysed by reverse zymography (Figure 7f). No significant differences were observed between the different EV conditions. After addition of EVs on HMEC-1 cells, the amounts of MMP2, MMP14, uPA, and TIMP2 transcripts were not significantly modulated between EV conditions (Figure 7g–j). Note that like proteins, the transcript amounts of MMP2 and uPA increased over time compared with the untreated condition. MMP2 transcript ratios increased in PDAC-derived EV (0.0117 ± 0.0014) and PDAC AG-9-derived EV (0.0128 ± 0.0002) conditions by 3.22- and 3.51-fold at time 48 h, respectively (untreated condition: 0.0036 ± 0.0001). uPA transcript increased in PDAC-derived EV (0.0026 ± 0.0001) and PDAC AG-9-derived EV (0.0031 ± 0.0001) conditions by 1.92-fold and 2.30-fold at time 48 h, respectively (untreated condition: 0.0013 ± 0.0003). As well as for protease gene expression, treatment of HMEC-1 cells with EVs modulated transcript levels over time, up to 48 h of incubation (Figure 7h–i). No significant differences in the gene expression levels of ITG subunits, RPSA receptor and TRPM7 ion channel were found between the different EV conditions. Compared to the untreated condition, as for PDAC cells (WT), the transcript level of the ITGβ3 increased in EV conditions by 3.86-fold (PDAC AG-9-derived EVs) and 3.40-fold (PDAC AG-9-derived EVs) respectively (Figure S6).

3.8 | In vitro effect of PDAC-derived EVs and PDAC AG-9-derived EVs on pseudotube formation and associated gene expression

Previous studies have shown that AG-9 stimulates in vitro and in vivo angiogenesis (Da Silva et al., 2018, Nannan et al., 2023). To study the effect of EVs on angiogenesis, HMEC-1 cells were seeded on Matrigel and pseudotube formation was analysed after 24 h of incubation. We found that, compared with control conditions, 10^9 EVs mL^{-1} significantly stimulated angiogenesis by increasing the numbers of nodes (1.10-fold increase for PDAC-derived EVs ($p < 0.01$ [**]) and 1.07-fold increase for PDAC AG-9-derived EVs ($p < 0.05$ [*]), junctions (1.09-fold increase for PDAC-derived EVs ($p < 0.01$ [**]) and 1.07-fold increase for PDAC AG-9-derived EVs ($p < 0.05$ [*]), segments (1.10-fold increase for PDAC-derived EVs ($p < 0.05$ [*]) and 1.08-fold increase for PDAC AG-9-derived EVs ($p < 0.05$ [*]) and mesh area (1.67-fold increase for PDAC-derived EVs ($p \leq 0.0001$ [****]) and 1.46-fold increase for PDAC AG-9-derived EVs ($p < 0.01$ [**]) (Figure 8a,b). No significant differences in the numbers of nodes, junctions and mesh area were found between PDAC-derived EV and PDAC AG-9-derived EV treatments. In all conditions, the mesh number showed no significant differences. Unlike the numbers of nodes, junctions, segments and mesh area, compared to control condition, isolated segment number in EV treated conditions were significantly reduced (0.67-fold increase with PDAC-derived EVs ($p \leq 0.0001$ [****]) and 0.81-fold increase with PDAC AG-9-derived EVs ($p < 0.05$ [*]) (Figure 8b). As shown in Figure 8a, the consequence of an increase in the number of nodes, junctions, segments and mesh area and the decrease in
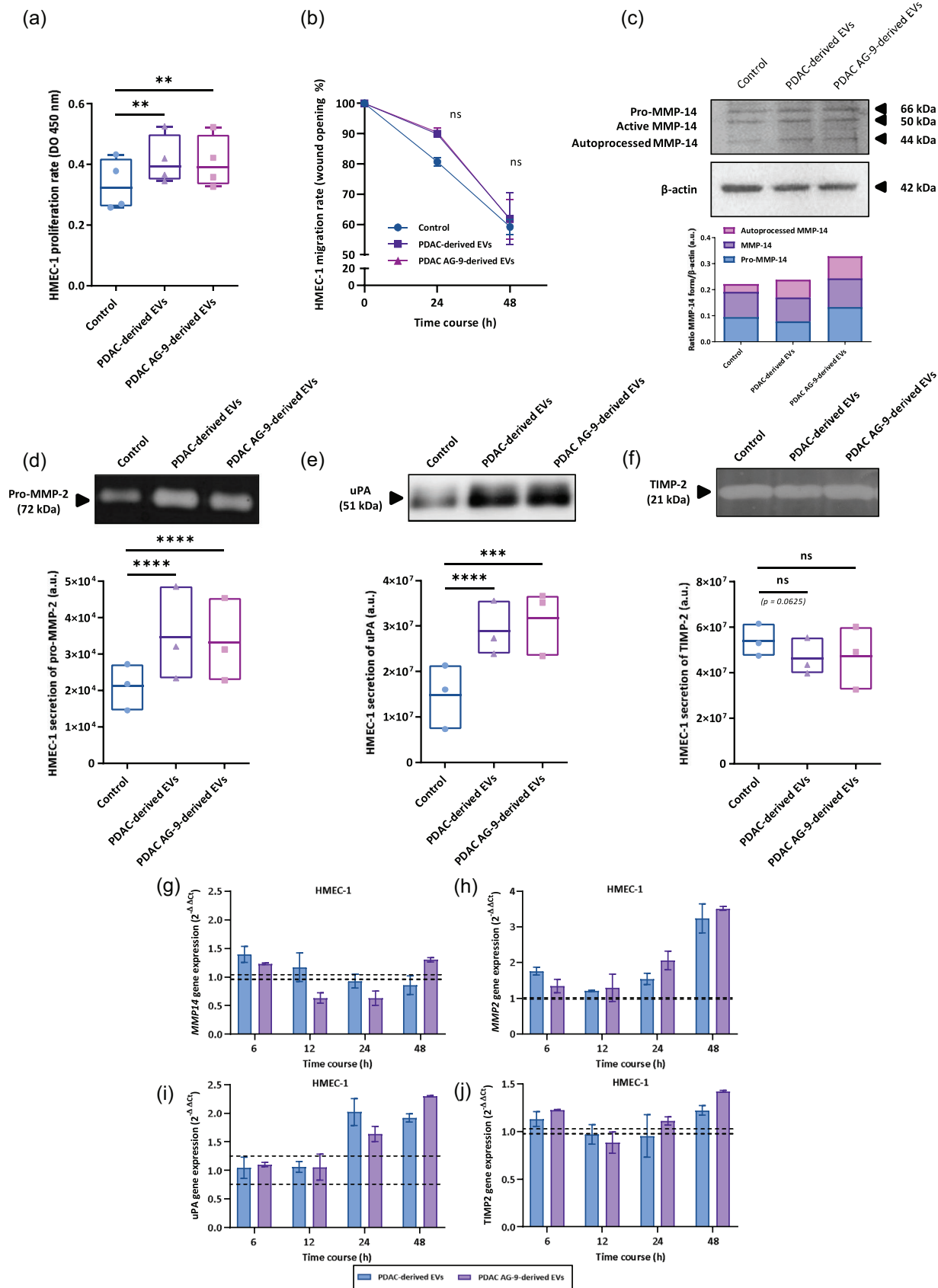
FIGURE 7 In vitro effect of PDAC-derived EVs and PDAC AG-9-derived EVs on angiogenesis and proteinase expression. (a) Proliferation of HMEC-1 cells after treatment with EVs (10^9 EVs mL^{-1}). Cell proliferation rate measurement by WST-1 assay at 72 h (box and whiskers; Min to Max.; $N = 4$, $n = 3$; **,

(Continues)

FIGURE 7 (Continued)

$p < 0.01$; Student's t test). (b) Migration of HMEC-1 cells after treatment with EVs (10^9 EVs mL^{-1}). Cell migration evaluation by scratch assay at different time points (mean ± SEM; $N = 3$, $n = 3$; ns, not significant; Mann-Whitney U test). (c) WB anti-MMP-14 on total protein extracted from HMEC-1 cells after 6 h of treatment with EVs (10^9 EVs mL^{-1}). β-actin was used as an internal control. Graph shows the ratio of MMP-14 form (autoprocessed MMP-14, MMP-14 and pro-MMP-14) and β-actin. (d) Pro-MMP-2 secretion by HMEC-1 cells after treatment with EVs (10^9 EVs mL^{-1}). Pro-MMP-2 secretion measurement by gelatin zymography after 48 h of incubation (box and whiskers; Min to Max.; $N = 3$, $n = 4$; ****, $p \leq 0.0001$; Mann-Whitney U test). (e) uPA secretion by HMEC-1 cells after treatment with EVs (10^9 EVs mL^{-1}). uPA secretion measurement by gelatin/plasminogen zymography after 48 h of incubation (box and whiskers; Min to Max.; $N = 3$, $n = 4$; ns, ***, $p < 0.001$, ****, $p \leq 0.0001$; Mann-Whitney U test). (f) TIMP-2 secretion by HMEC-1 after treatment with EVs (10^9 EVs mL^{-1}). TIMP-2 secretion measurement by reverse zymography after 48 h of incubation (box and whiskers; Min to Max.; $N = 3$, $n = 4$; ns; Mann-Whitney U test). (g–j) Quantitative RT-PCR analysis of MMP2, uPA, TIMP2 and MMP14 mRNA at different time points after treatment of HMEC-1 cells with EVs (10^9 EVs mL^{-1}). eEF1a1 was used as an internal standard (the minimum and maximum SEM from control condition [time course of 0 h] are shown on the graphs by dashed lines; mean ± SEM; $N = 2$, $n = 3$). EV, extracellular vesicles; PDAC, pancreatic ductal adenocarcinoma.

the number of isolated segments results in a denser and more complex pseudotube network. Among all the factors associated with angiogenesis (ANXA1, VEGFA, TRAF6, EGFR, PDGFβ and CXCL8), analysed by RT-qPCR, no significant change in gene expression was observed over time (Figure 8c).

3.9 | Immunodetection of cell surface RPSA on endothelial cells after PDAC-derived EVs and PDAC AG-9-derived EVs

We previously showed that the RPSA elastin receptor was present in EVs at transcript and protein levels (Figure 1j-l). PDAC AG-9-derived EV treatment of PDAC cells stimulated RPSA protein expression (Figure 6e). To study the involvement of the PDAC EVs on RPSA localisation on HMEC-1 cells, immunostainings with anti-RPSA antibody in non-permeabilized conditions were realised after 24 h EV treatments. We made confocal images of HMEC-1 cell surfaces. Compared to PDAC-derived EVs, a 24 h treatment of HMEC-1 cells with 10^9 PDAC-derived EVs or 2.10^9 PDAC AG-9-derived EVs caused an increase on HMEC-1 cell surface RPSA elastin receptor (Figure 9a). Quantification of HMEC-1 cell surface RPSA showed a significant increase with PDAC-derived EVs (4.51 ± 2.45-fold; $p \leq 0.0001$ [****]) and PDAC-AG-9 derived EVs (8.06 ± 2.51-fold; $p \leq 0.0001$ [****]) (Figure 9b). PDAC AG-9-derived EVs significantly increase HMEC-1 cell surface RPSA elastin receptor compared to PDAC-derived EVs ($p < 0.01$ [$$]).

3.10 | In vitro and in vivo optical imaging of labelled PDAC-derived EVs and PDAC AG-9-derived EVs in a mouse model

To study the in vivo biodistribution of EVs in a mouse model, due to the lack of sensitivity to detect eGFP-related fluorescence, we relied on the detection of BLI due to the enzymatic activity of FLuc in the presence of D-luciferin. To follow the biodistribution of EVs intravenously injected into the tail vein of mice, we followed the protocol shown in Figure 10a. Mice were s.c. injected with 5×10^6 PDAC cells into the right flank and they were randomly divided into three groups (NaCl [0.9%; 100 μL] [group 1], PDAC-derived EVs [group 3] and PDAC AG-9-derived EVs [group 4]) at day 30. EVs were isolated from conditioned media obtained from PDAC cells (eGFP-FLuc$^+$). Prior to performing the in vivo assay, the BLI of EVs was detected with an IVIS Spectrum imaging system. To determine the minimal amount of EVs allowing the detection of bioluminescence, two EV quantities (3×10^9 and 7×10^9 EVs) were deposited in 96-well plates before the addition of D-luciferin. BLI signal intensities showed that the FLuc level and BLI signals increased in a dose-dependent manner (Figure 10b). WB analysis further confirmed the presence of FLuc protein in EVs (Figure 1h). Based on these results we decided to use 7×10^9 EV for in vivo experiment. Groups 2, 3 and 4 received an intravenous injection of 3.5×10^{11} EVs kg^{-1}. 0.9% NaCl was injected in group 1 (control mice). D-Luciferin was intravenously injected at the same time as EVs or 0.9% NaCl and, after 30 min, a second injection of substrate was done.

Group 1 undergoing 0.9% NaCl injection did not allow BLI detection and was used to determine the threshold level. The total photon flux (p s^{-1}) for this group 1 remained constant over time and in the different body parts (body, thorax, abdomen, head and tumour regions). The injection of a constant amount of EVs in groups 2, 3 and 4 resulted in a different biodistribution of EVs within the different body regions. The EV biodistribution varied also as a function of postinjection time. BLI signal was detected as early as 5 min after injection in groups 2, 3, and 4. In groups 3 and 4 (PDAC tumour-bearing mice), BLI signal intensity was most intense in the head and thorax regions. Interestingly, BLI signal is most persistent for group 4 in the thorax region compared to other groups. In group 2 (tumour-free mice), BLI signals were visualised in the head and abdomen regions (Figure 10c,d). These signals were more pronounced in head and abdomen regions compared to other groups. As early as 5 min after the injection of EVs in group 2, their EV biodistribution was maximum in the whole body. In contrast, the BLI signal remained weaker in the thorax, similar to the level observed for group 3, PDAC-derived EVs. After 40 min postinjection, the BLI signal changed in location and intensity illustrating a redistribution of EVs (Figure 10c, lower panel). In group 3, the BLI
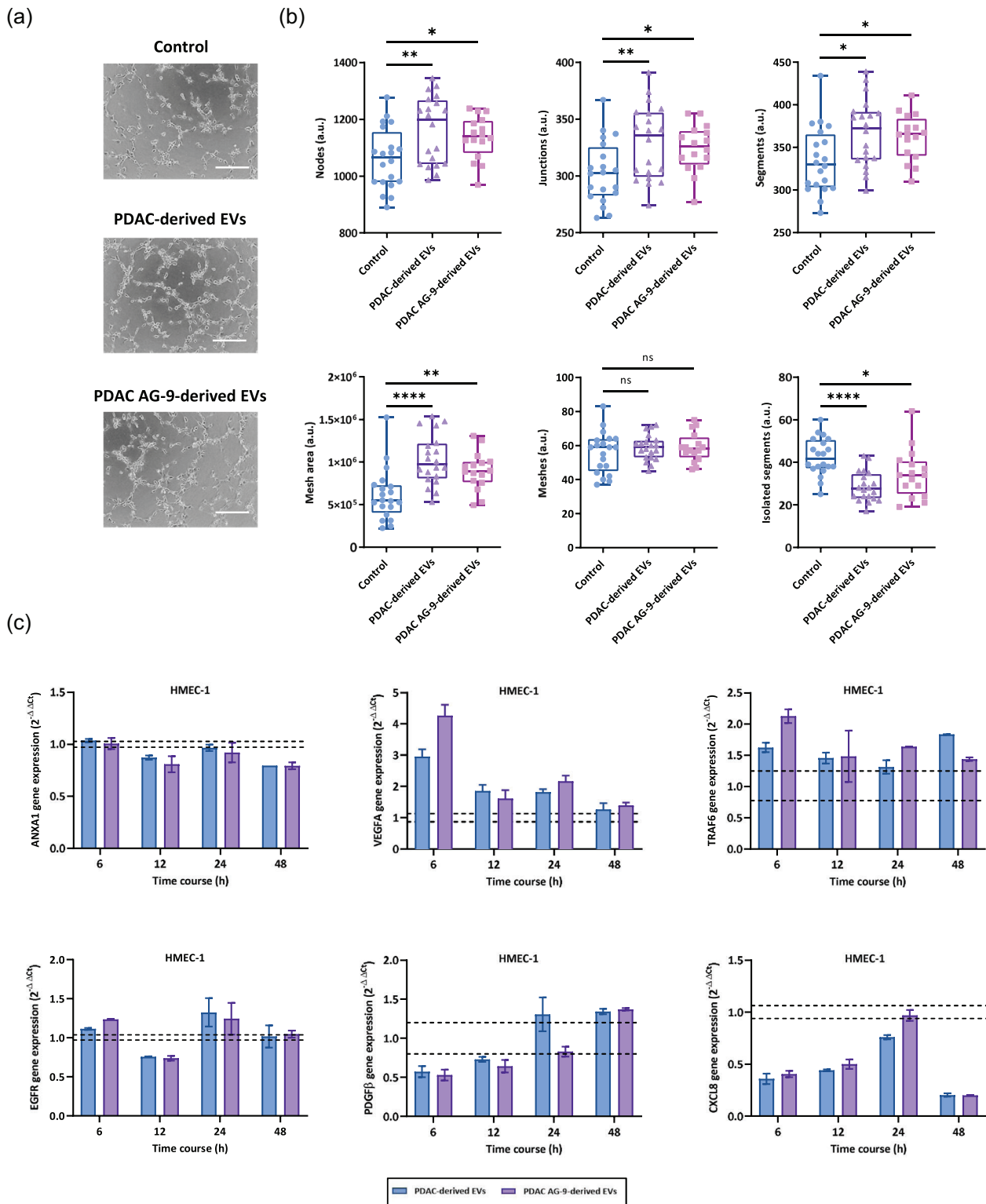
FIGURE 8 In vitro effect of PDAC-derived EVs and PDAC AG-9-derived EVs on pseudotube formation and associated gene expression. HMEC-1 pseudotube formation after treatment with EVs (10^9 EVs mL^{-1}) was estimated after 24 h of incubation. (a) Phase contrast images of HMEC-1 pseudotube formation. Scale bar: 200 µm. (b) The number of nodes, junctions, meshes, isolated segments, mesh area and segments were measured with ImageJ software via Angiogenesis Analyser plugin (box and whiskers; Min to Max.; data from one experiment, representative of three independent experiments, are shown;, $N = 3$, $n = 5$; ns, not significant, * $p < 0.05$, ** $p < 0.01$, **** $p \leq 0.0001$; *Mann-Whitney U* test). (c) Quantitative RT-PCR analysis of *ANXA1*, *VEGFA*, *TRAF6*, *EGFR*, *PDGFβ* and *CXCL8* mRNA at different time points after treatment of HMEC-1 cells with EVs (10^9 EVs mL^{-1}). *eEF1a1* was used as an internal standard (the minimum and maximum SEM from control condition [time course of 0 h] are shown on the graphs by dashed lines; mean ± SEM; $N = 2$, $n = 3$). EV, extracellular vesicles; PDAC, pancreatic ductal adenocarcinoma.

HMEC-1

(a)

RPSA

Control

PDAC-derived EVs
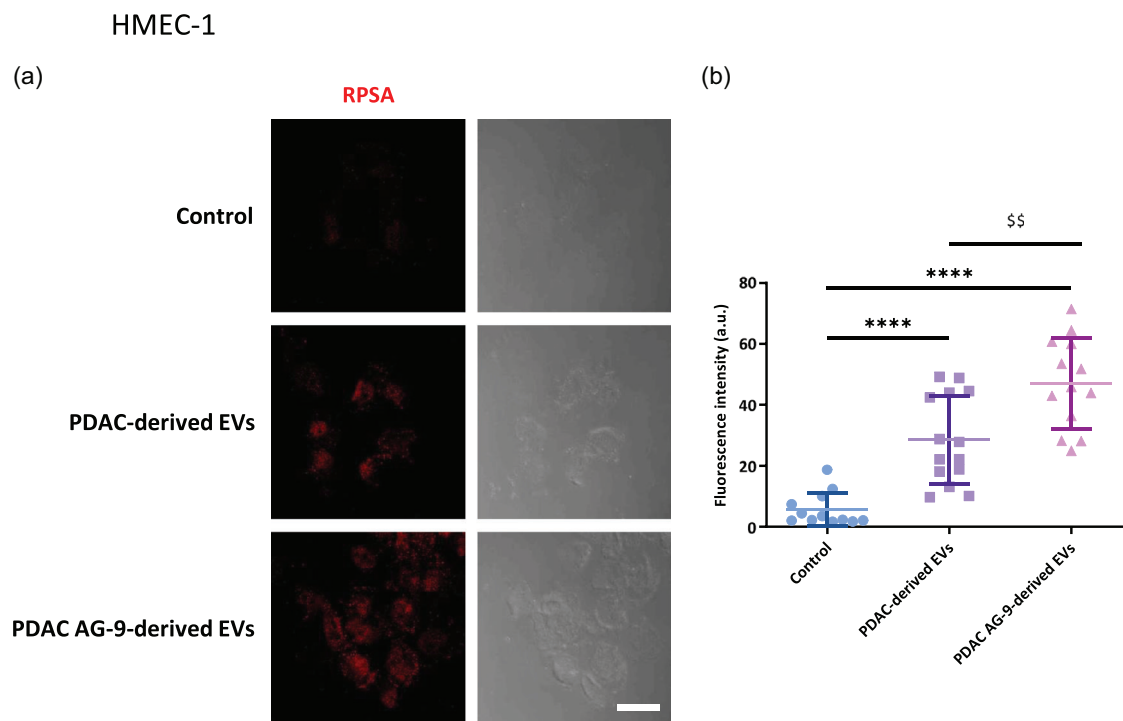
PDAC AG-9-derived EVs

(b)

FIGURE 9 Immunodetection of cell surface RPSA on endothelial cells after PDAC-derived EVs and PDAC AG-9-derived EVs. (a) Confocal images of HMEC-1 immunostaining with anti-RPSA antibody. Scale bar: 20 μm. (b) Quantification of anti-RPSA signal on HMEC-1 cell surface (scatter dot plots; mean ± SD; $N = 2$, $n = 13$; **** $p \leq 0.0001$, when we compared control to EVs; \$\$, $p < 0.01$, when we compared PDAC-derived EVs to PDAC AG-9-derived EVs; *Mann-Whitney U* test). EV, extracellular vesicles; PDAC, pancreatic ductal adenocarcinoma; RPSA, ribosomal protein SA.

signal remained relatively constant throughout the body and as a function of postinjection time. Forty min after injection, an accumulation of BLI signals was detectable in the tumour. In group 4 (PDAC AG-9-derived EVs), the maximum intensity of BLI was detected in the thorax region, probably in the lungs as early as 5 min after injection (Figure 10c,d). Group 4 showed predominant accumulation in the thorax region compared with group 3. After 40 min, BLI signal intensities decreased sharply in this area and a complete redistribution of PDAC AG-9-derived EVs was then demonstrated. Interestingly, we observe an increasing BLI signal in the abdomen region in group 4. The BLI signal intensity in the tumour reached levels similar to those detected in group 3. At 40 min, an increase of BLI signals was found in the tumour site for groups 3 and 4 when compared to the 5 min time point.

4 | DISCUSSION

Pancreatic cancer is one of the most common malignancies. The incidence of PDAC continues to increase and is projected to be the second most common cancer in terms of mortality by 2030 (Rahib et al., 2014). The lack of effective treatment and diagnostic methods, resulting in a poor prognosis associated with a very high mortality rate. To date, the pathogenesis and mechanisms of progression of pancreatic cancer have been poorly characterised. The objective of our work was to highlight the influence of EVs in this pathology and upstream, the importance of the microenvironment on the regulation of their biological activities.

To investigate the influence of the microenvironment on EV-regulated biological activities in PDAC, we developed a cellular model based on the expression of two in vivo and in vitro imaging markers, eGFP and FLuc proteins. Expression of eGFP by PDAC cells (eGFP-FLuc^{+}) did not allow us to track fluorescence within the released EVs. Although containing the transcript and eGFP protein, evidenced by in NTA analysis, confocal microscopy or videomicroscopy, no fluorescent EVs were detected. It is challenging to investigate conventional fluorescent proteins in EV research (Huotari & Helenius, 2011; Shinoda et al., 2018). Actually, a pH-sensitive GFP; pHluorin2 is a variant for a significant improvement in the change of GFP pH (Mahon, 2011). Since years, numerous researchers have used pHluorin in EV research (Verweij et al., 2018, Verweij et al., 2019). By contrast, FLuc expression by these cells allowed us to track PDAC progression under the influence of AG-9 in an in vivo model (Nannan et al., 2023) but also the fate of EVs in vitro and in vivo, in particular by tracing transcripts and proteins in qPCR and immunostaining in PDAC cells and stromal cells. In addition, FLuc^{+} EVs allowed us to follow in vivo their biodistribution and kinetics after intravenous injection. We demonstrated that depending on the conditions of EV biogenesis, by culturing PDAC cells
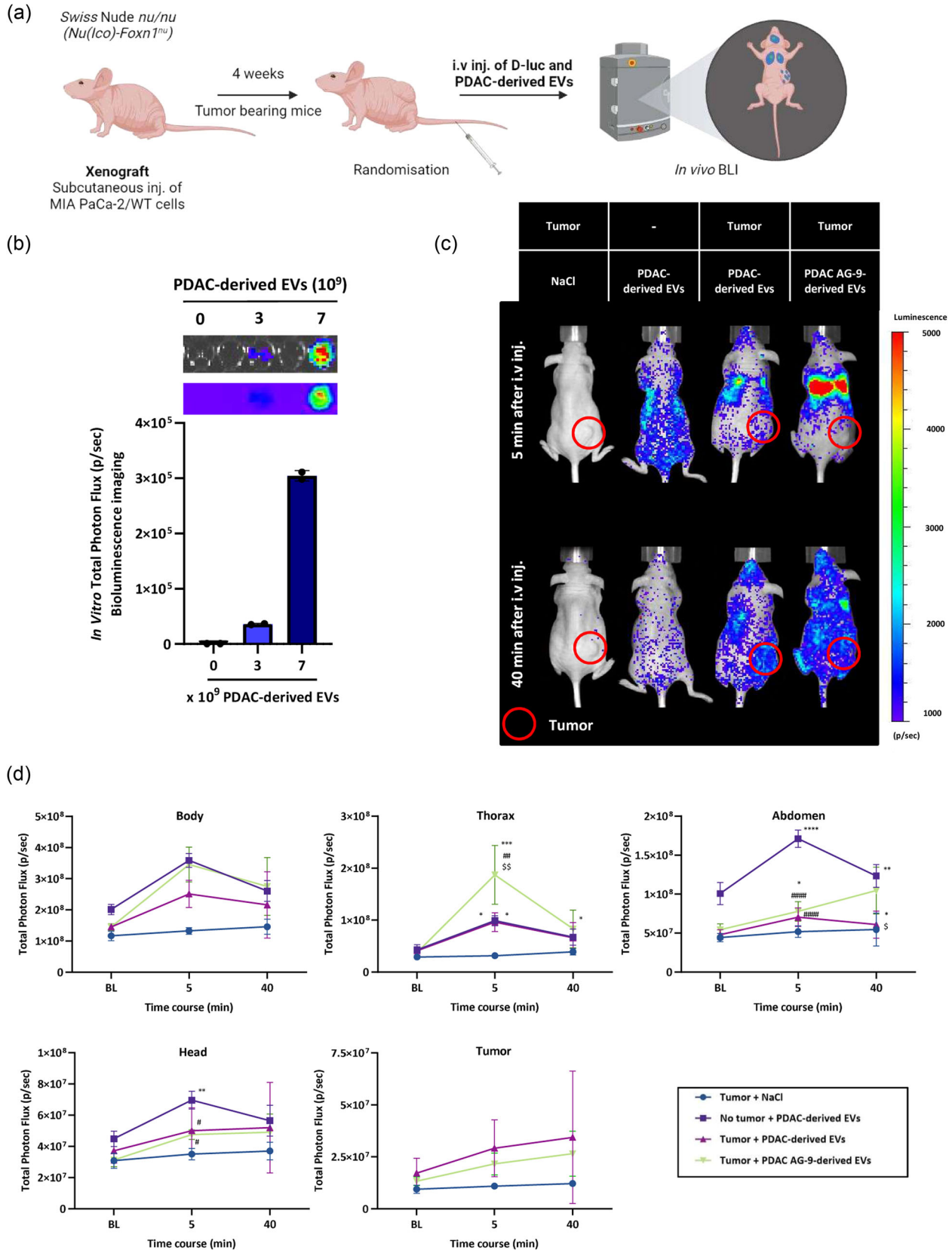
FIGURE 10 In vitro and in vivo optical imaging of labelled PDAC-derived EVs and PDAC AG-9-derived EVs in a mouse model. (a) Workflow representative of the following protocol. Created with BioRender.com (b) In vitro bioluminescence activity of FLuc in PDAC-derived EVs and total photon flux (p s^{-1}). (c) Representative in vivo BLI biodistribution of EVs (3.5×10^{11} EVs kg^{-1}) intravenously administered to naïve or PDAC tumour-bearing mice. (d) Graphs show quantification of EV signals (p s^{-1}) in body, head, thorax, abdomen and tumour regions in mice (mean ± SD; $n = 3$; *, $p < 0.05$, **, $p < 0.01$, ***,

FIGURE 10   (Continued)

$p < 0.001$, ****, $p \leq 0.0001$, when we compared group 1 to other groups; #, $p < 0.05$, ##, $p < 0.01$, ####, $p \leq 0.0001$, when we compared group 2 to group 3 and 4; $, $p < 0.05$, $$, $p < 0.01$, when we compared group 3 to group 4; *2-way ANOVA* test). EV, extracellular vesicles; PDAC, pancreatic ductal adenocarcinoma; RPSA, ribosomal protein SA.

(eGFP-FLuc$^+$) in the presence or absence of AG-9, the tissue orientation of EVs and their maintenance in these organs is conditioned by the initial microenvironment of the tumour cells (André-Grégoire et al., 2022; Gangadaran et al., 2017; Gupta et al., 2020; Lai et al., 2014; Takahashi et al., 2013; Wu et al., 2020; Zaborowski et al., 2019; Zhu et al., 2018). The concentrations of EVs measured by the NTA system are similar to those previously published (Sarcar et al., 2022). If at first, we tested the concentrations of EVs measured in our various experimental conditions, we made the choice to carry out a normalised and standardised study. By performing all the experiments with a constant concentration of EVs, we wished to highlight the influence of the microenvironment on the conditioning of EVs from PDAC and to evaluate their impacts in tumour progression. Starting from a standardised concentration thanks to the quantification by the NTA method for our two experimental conditions, we obtain either no significant modification or modulation of the biological activities according to the origin of the EVs. Focusing on EV uptake, at a concentration of 10^9 EVs mL^{-1}, the detection of the eGFP and FLuc markers is little deregulated. The levels of eGFP and FLuc do not show significant changes between EV groups, but we found increased amounts of mRNA for both markers in recipient cells. From these results, the tracking of GFP and FLuc RNAs and their stability have not been further investigated. This could be the subject of a future paper. The example of uptake in relation to the other activities studied in our work may illustrate that simply by doubling the amount of EVs released, the microenvironment potentially modulates many biological activities via EVs.

The choice of a concentration at 10^9 EVs mL^{-1} was defined according to several findings, which is in the same range as in previous studies (Korvenlaita et al., 2023, Nguyen et al., 2022, Grisard et al., 2022). As previously reported, we made chose to work with a constant concentration of total proteins extracted from EVs (Jung et al., 2022; Ludwig et al., 2022; Sarcar et al., 2022). Since the content of EVs is modulated according to the microenvironment, standardisation by the number of EVs seemed to us to be more robust and representative of the physiopathological context. In this study, we established a link between the amount of EVs and the amount of protein extracted from them. 10^9 EVs resulted in approximately 5 µg of total proteins. Concentrations of 1–10 µg mL^{-1} or even 20 µg mL^{-1} are regularly used in biological tests in many studies (Bonsergent et al., 2021).

In our study, among the elements carried is the RPSA receptor. RPSA is present in the form of transcript and protein in EVs. We have shown that EVs transfer the RPSA receptor to HMEC-1 endothelial cells. Indeed, upon contact with EVs, the RPSA receptor is detected on the surface of HMEC-1 cells. HMEC-1 cells switch from an RPSA$^-$ to an RSPA$^+$ phenotype. In fact, we can assume that these HMEC-1 cells with a significant amount of membrane RPSA make these cells much more sensitive to the protumoural AG-9. The AG-9 not only directly stimulates tumour progression, via its RSPA receptor, by increasing cell proliferation, angiogenesis but also indirectly via EVs, by stimulating their release, modulating their content and ultimately biological processes. The presence of EVs stimulates angiogenesis. In the presence of EVs, the number of nodes and segments as well as the mesh area increased significantly. Among the set of peritumoural stromal cells are PSCs which are a target for EVs. In a future study, it would be wise to investigate the intercellular communication between PDAC and PSCs and possibly, from PSCs to PDAC cells. PDAC tumours are characterised by the presence of activated PSCs, involved in the desmoplastic reaction. These cells represent key players in tumour stroma, as they actively participate in the development and progression of the disease. Numerous studies suggest that reprogramming these stellate cells to a quiescent phenotype is a promising strategy to restore the characteristics of a healthy pancreas (Auwercx et al., 2022, Das et al., 2020, Shi et al., 2019).

In the present study, we have shown that the microenvironment has an impact on EV secretion, uptake and content. Since 1999, with the definition of the concept of matrikines, products of ECM degradation regulating biological processes (Maquart et al., 1999), we have demonstrated the influence of EDPs on cancer. These peptides exert a protumour activity. Thus, we have previously shown that the AG-9 stimulates PDAC growth in vivo (Nannan et al., 2023). In this new study, we show that AG-9 modulates EV biogenesis, intercellular communication through EVs. We have previously demonstrated that extracellular matrix degradation products like AG-9 induce the release of Hsp90-containing EVs and proteinases into the extracellular space (Brassart et al., 2019). Since EVs stimulate angiogenesis, cell proliferation and proteinase secretion, our data suggest that matrikines, such as AG-9, released into the microenvironment, may induce the release of higher extracellular vesicles amount facilitating tumour growth. Plasma membrane display many receptors such as integrins. As described in the introduction section, the integrin expression pattern may predict organ-specific metastatic. We hypothesise that AG-9 may have an impact on the EV composition. It would be interesting to focus EV composition using different modalities (proteomic analysis, RNA sequencing or mass spectroscopy) and to study EV adhesion to different matricial supports, such as collagen, using atomic force macroscopy.

Bioengineering is a valuable tool in research for EV study strategies in biogenesis, secretion, transfer biodistribution, uptake and functional transfer. With recent advances in microscopy techniques, novel EV labelling strategies allow numerous study strategies in subcellular and body-wide resolution (Verweij et al., 2021).

For cancer research, the in vivo visualisation can provide a foundation for developing EV-based drug delivery systems as we could observed the targeting ability of EVs to PDAC tumours in our in vivo mouse model with reporter gene-based optical imaging with eGFP and FLuc protein EV reporters (Nannan et al., 2023). Correlative microscopy combines in our study confocal microscopy and SEM. This set-up allows the detection at the plasma membrane of receiving cells the presence of EVs and their uptake resulting of dynamic transfer of our reporter proteins (eGFP and FLuc). Combining multiple reporter proteins and high-spatial resolution, we could improve the follow-up of dynamic molecular processes involving EVs. Further studies need to be performed to determine what happens after EV uptake in terms of the fusion events or transporter systems necessary for delivery. This mechanism is unknown to date.

In our PDAC mouse model, we observed a more important accumulation of PDAC AG-9-derived EVs in the region of thorax compared to other groups suggesting a local retention, a concept of organotropism. Since decade, we know that the microenvironment plays a major role in EV distribution and function (Hoshino et al., 2015). The ECM and biological barriers impact EV diffusion and their role in physiological and pathological conditions. During PDAC disease, the favourite place of metastasis are lungs. Metastasis is a dynamic process implicating dissemination of primary tumour cells to distant sites in the body. Reports indicate the implication of fluids and other mechanisms in tumour transit (Follain et al., 2020) and the role of EV in the capacity to form premetastatic niches (Becker et al., 2016, Bobrie et al., 2012; Ghoroghi et al., 2021; Jerabkova-Roda et al., 2022). As we have not fully elucidated how microenvironment and AG-9 influence cancer progression via EVs, future studies will be required to identify the mechanism implicated in PDAC cancer progression. While the use of a mouse xenograft PDAC model allows easy monitoring of tumour growth, it also has its drawbacks such as the absence of the immune system. Pancreatitis is responsible for an inflammation widely described in the literature in connection with the induction of pancreatic cancer. Aware of the importance of the involvement of the immune system in this pathology, in the future, the use of a non-immunocompromised mouse model could be considered with an appropriate orthotopic model.

To conclude, our data demonstrate the protumoural potential of tumour-derived EVs from PDAC under the influence of microenvironment on their effects on tumour progression (tumour growth and angiogenesis). In vitro, tumour-derived EVs increase cell proliferation and migration and promote pseudotube formation. We successfully observed the in vivo biodistribution of tumour-derived EVs through bioengineering and their ability to target tumours. They are potential candidates for targeted drug delivery and modulation of tumour progression. They constitute a new generation of therapeutic tools without cells, merging oncology with genic therapy, useful in biomedical and biotechnological applications on the development of new nanoparticles and instrumentations for cancer imaging.

4.1 | Geolocation information

- CNRS UMR 7369 Matrice Extracellulaire et Dynamique Cellulaire, Université de Reims Champagne Ardenne, Reims, France (49.228014N, 4.015938E).
- KU Leuven, Department of Imaging and Pathology/Biomedical MRI, Leuven, Belgium (50.878799N, 4.673550E).

AUTHOR CONTRIBUTIONS
Lise Nannan, Salomé Decombis, Willy Gsell, Sandra Audonnet, Sylvie Brassart-Pasco, Uwe Himmelreich and Bertrand Brassart designed, performed, and analysed all of the experiments. TEM was performed by Jean Michel. Correlative microscopy was performed by Christine Terryn. Bertrand Brassart wrote the paper with Lise Nannan, Bertrand Brassart, Sylvie Brassart-Pasco, Willy Gsell and Uwe Himmelreich provided essential editorial oversight and critical review.

CONFLICT OF INTEREST STATEMENT

None of the authors have any conflict to declare.

DATA AVAILABILITY STATEMENT

The data that support the findings of this study are available from the corresponding author upon reasonable request.

ORCID

Bertrand Brassart https://orcid.org/0000-0002-4879-6832

REFERENCES

Al-Nedawi, K., Meehan, B., Micallef, J., Lhotak, V., May, L., Guha, A., & Rak, J. (2008). Intercellular transfer of the oncogenic receptor EGFRvIII by microvesicles derived from tumour cells. *Nature Cell Biology*, *10*(5), 619–624.

André-Grégoire, G., Maghe, C., Douanne, T., Rosińska, S., Spinelli, F., Thys, A., Trillet, K., Jacobs, K. A., Ballu, C., Dupont, A., Lyne, A. M., Cavalli, F. M. G., Busnelli, I., Hyenne, V., Goetz, J. G., Bidère, N., & Gavard, J. (2022). Inhibition of the pseudokinase MLKL alters extracellular vesicle release and reduces tumor growth in glioblastoma. *Iscience*, *25*(10), 105118.

Auwercx, J., Kischel, P., Lefebvre, T., Jonckheere, N., Vanlaeys, A., Guénin, S., Radoslavova, S., Van Seuningen, I., Ouadid-Ahidouch, H., Kocher, H. M., Dhennin-Duthille, I., & Gautier, M. (2022). TRPM7 modulates human pancreatic stellate cell activation. *Cells*, *11*(14), 2255.

Becker, A., Thakur, B. K., Weiss, J. M., Kim, H. S., Peinado, H., & Lyden, D. (2016). Extracellular vesicles in cancer: Cell-to-cell mediators of metastasis. *Cancer Cell*, *30*(6), 836–848.

Betre, H., Ong, S. R., Guilak, F., Chilkoti, A., Fermor, B., & Setton, L. A. (2006). Chondrocytic differentiation of human adipose-derived adult stem cells in elastin-like polypeptide. *Biomaterials*, *27*(1), 91–99.

Bobrie, A., Krumeich, S., Reyal, F., Recchi, C., Moita, L. F., Seabra, M. C., Ostrowski, M., & Théry, C. (2012). Rab27a supports exosome-dependent and -independent mechanisms that modify the tumor microenvironment and can promote tumor progression. *Cancer Research*, *72*(19), 4920–4930.

Bonsergent, E., Grisard, E., Buchrieser, J., Schwartz, O., Théry, C., & Lavieu, G. (2021). Quantitative characterization of extracellular vesicle uptake and content delivery within mammalian cells. *Nature Communications*, *12*(1), 1864.

Brassart, B., Da Silva, J., Donet, M., Seurat, E., Hague, F., Terryn, C., Velard, F., Michel, J., Ouadid-Ahidouch, H., Monboisse, J. C., Hinek, A., Maquart, F. X., Ramont, L., & Brassart-Pasco, S. (2019). Tumour cell blebbing and extracellular vesicle shedding: Key role of matrikines and ribosomal protein SA. *British Journal of Cancer*, *120*(4), 453–465.

Brassart, B., Gomez, D., De Cian, A., Paterski, R., Montagnac, A., Qui, K. H., Temime-Smaali, N., Trentesaux, C., Mergny, J. L., Gueritte, F., & Riou, J. F. (2007). A new steroid derivative stabilizes g-quadruplexes and induces telomere uncapping in human tumor cells. *Molecular Pharmacology*, *72*(3), 631–640.

Brassart, B., Randoux, A., Hornebeck, W., & Emonard, H. (1998). Regulation of matrix metalloproteinase-2 (gelatinase A, MMP-2), membrane-type matrix metalloproteinase-1 (MT1-MMP) and tissue inhibitor of metalloproteinases-2 (TIMP-2) expression by elastin-derived peptides in human HT-1080 fibrosarcoma cell line. *Clinical & Experimental Metastasis*, *16*(6), 489–500.

Consortium, EV-TRACK, Van Deun, J., Mestdagh, P., Agostinis, P., Akay, Ö., Anand, S., Anckaert, J., Martinez, Z. A., Baetens, T., Beghein, E., Bertier, L., Berx, G., Boere, J., Boukouris, S., Bremer, M., Buschmann, D., Byrd, J. B., Casert, C., Cheng, L., … Hendrix, A. (2017). EV-TRACK: Transparent reporting and centralizing knowledge in extracellular vesicle research. *Nature Methods*, *14*(3), 228–232.

Costa-Silva, B., Aiello, N. M., Ocean, A. J., Singh, S., Zhang, H., Thakur, B. K., Becker, A., Hoshino, A., Mark, M. T., Molina, H., Xiang, J., Zhang, T., Theilen, T. M., García-Santos, G., Williams, C., Ararso, Y., Huang, Y., Rodrigues, G., Shen, T. L., … Lyden, D. (2015). Pancreatic cancer exosomes initiate pre-metastatic niche formation in the liver. *Nature Cell Biology*, *17*(6), 816–826.

Das, S., Shapiro, B., Vucic, E. A., Vogt, S., & Bar-Sagi, D. (2020). Tumor cell-derived IL1β promotes desmoplasia and immune suppression in pancreatic cancer. *Cancer Research*, *80*(5), 1088–1101.

Da Silva, J., Lameiras, P., Beljebbar, A., Berquand, A., Villemin, M., Ramont, L., Dukic, S., Nuzillard, J. M., Molinari, M., Gautier, M., Brassart-Pasco, S., & Brassart, B. (2018). Structural characterization and *in vivo* pro-tumor properties of a highly conserved matrikine. *Oncotarget*, *9*(25), 17839–17857.

DiGiacomo, V., & Meruelo, D. (2016). Looking into laminin receptor: Critical discussion regarding the non-integrin 37/67-kDa laminin receptor/RPSA protein. *Biological Reviews of the Cambridge Philosophical Society*, *91*(2), 288–310.

Donet, M., Brassart-Pasco, S., Salesse, S., Maquart, F. X., & Brassart, B. (2014). Elastin peptides regulate HT-1080 fibrosarcoma cell migration and invasion through an Hsp90-dependent mechanism. *British Journal of Cancer*, *111*(1), 139–148.

Follain, G., Herrmann, D., Harlepp, S., Hyenne, V., Osmani, N., Warren, S. C., Timpson, P., & Goetz, J. G. (2020). Fluids and their mechanics in tumour transit: Shaping metastasis. *Nature Reviews Cancer*, *20*(2), 107–124.

Gangadaran, P., Li, X. J., Lee, H. W., Oh, J. M., Kalimuthu, S., Rajendran, R. L., Son, S. H., Baek, S. H., Singh, T. D., Zhu, L., Jeong, S. Y., Lee, S. W., Lee, J., & Ahn, B. C. (2017). A new bioluminescent reporter system to study the biodistribution of systematically injected tumor-derived bioluminescent extracellular vesicles in mice. *Oncotarget*, *8*(66), 109894–109914.

Ghoroghi, S., Mary, B., Larnicol, A., Asokan, N., Klein, A., Osmani, N., Busnelli, I., Delalande, F., Paul, N., Halary, S., Gros, F, Fouillen, L., Haeberle, A. M., Royer, C., Spiegelhalter, C., André-Grégoire, G., Mittelheisser, V., Detappe, A., Murphy, K., … Hyenne, V. (2021). Ral GTPases promote breast cancer metastasis by controlling biogenesis and organ targeting of exosomes. *Elife*, *10*, e61539.

Grisard, E., Nevo, N., Lescure, A., Doll, S., Corbé, M., Jouve, M., Lavieu, G., Joliot, A., Nery, E. D., Martin-Jaular, L., & Théry, C. (2022). Homosalate boosts the release of tumour-derived extracellular vesicles with protection against anchorage-loss property. *Journal of Extracellular Vesicles*, *11*(7), e12242.

Gupta, D., Liang, X., Pavlova, S., Wiklander, O. P. B., Corso, G., Zhao, Y., Saher, O., Bost, J., Zickler, A. M., Piffko, A., Maire, C. L., Ricklefs, F. L., Gustafsson, O., Llorente, V. C., Gustafsson, M. O., Bostancioglu, R. B., Mamand, D. R., Hagey, D. W., Görgens, A., … El Andaloussi, S. (2020). Quantification of extracellular vesicles *in vitro* and *in vivo* using sensitive bioluminescence imaging. *Journal of Extracellular Vesicles*, *9*(1), 1800222.

Gurung, S., Perocheau, D., Touramanidou, L., & Baruteau, J. (2021). The exosome journey: from biogenesis to uptake and intracellular signalling. *Cell Communication and Signaling*, *19*(1), 47.

Hoshino, A., Costa-Silva, B., Shen, T. L., Rodrigues, G., Hashimoto, A., Tesic Mark, M., Molina, H., Kohsaka, S., Di Giannatale, A., Ceder, S., Singh, S., Williams, C., Soplop, N., Uryu, K., Pharmer, L., King, T., Bojmar, L., Davies, A. E., Ararso, Y., … Lyden, D. (2015). Tumour exosome integrins determine organotropic metastasis. *Nature*, *527*(7578), 329–335.

Houghton, A. M., Mouded, M., & Shapiro, S. D. (2011). Consequences of elastolysis. In W. Parks, & R. Mecham (Eds.), *Extracellular matrix degradation* (pp. 217–249). Springer.

Huet, E., Brassart, B., Cauchard, J. H., Debelle, L., Birembaut, P., Wallach, J., Emonard, H., Polette, M., & Hornebeck, W. (2002). Cumulative influence of elastin peptides and plasminogen on matrix metalloproteinase activation and type I collagen invasion by HT-1080 fibrosarcoma cells. *Clinical & Experimental Metastasis*, *19*(2), 107–117.

Huotari, J., & Helenius, A. (2011). Endosome maturation. *The EMBO Journal*, *30*(17), 3481–3500.

Jerabkova-Roda, K., Dupas, A., Osmani, N., Hyenne, V., & Goetz, J. G. (2022). Circulating extracellular vesicles and tumor cells: sticky partners in metastasis. *Trends in Cancer*, *8*(10), 799–805.

Jung, D., Shin, S., Kang, S. M., Jung, I., Ryu, S., Noh, S., Choi, S. J., Jeong, J., Lee, B. Y., Kim, K. S., Kim, C. S., Yoon, J. H., Lee, C. H., Bucher, F., Kim, Y. N., Im, S. H., Song, B. J., Yea, K., & Baek, M. C. (2022). Reprogramming of T cell-derived small extracellular vesicles using IL2 surface engineering induces potent anti-cancer effects through miRNA delivery. *Journal of Extracellular Vesicles*, *11*(12), e12287.

Kim, S. M., Yang, Y., Oh, S. J., Hong, Y., Seo, M., & Jang, M. (2017). Cancer-derived exosomes as a delivery platform of CRISPR/Cas9 confer cancer cell tropism-dependent targeting. *Journal of Controlled Release*, *266*, 8–16.

Korvenlaita, N., Gómez-Budia, M., Scoyni, F., Pistono, C., Giudice, L., Eamen, S., Loppi, S., de Sande, A. H., Huremagic, B., Bouvy-Liivrand, M., Heinäniemi, M., Kaikkonen, M. U., Cheng, L., Hill, A. F., Kanninen, K. M., Jenster, G. W., van Royen, M. E., Ramiro, L., Montaner, J., … Malm, T. (2023). Dynamic release of neuronal extracellular vesicles containing miR-21a-5p is induced by hypoxia. *Journal of Extracellular Vesicles*, *12*(1), e12297.

Lai, C. P., Mardini, O., Ericsson, M., Prabhakar, S., Maguire, C., Chen, J. W., Tannous, B. A., & Breakefield, X. O. (2014). Dynamic biodistribution of extracellular vesicles in vivo using a multimodal imaging reporter. *ACS Nano*, *8*(1), 483–494.

Lefebvre, T., Rybarczyk, P., Bretaudeau, C., Vanlaeys, A., Cousin, R., Brassart-Pasco, S., Chatelain, D., Dhennin-Duthille, I., Ouadid-Ahidouch, H., Brassart, B., & Gautier, M. (2020). TRPM7/RPSA complex regulates pancreatic cancer cell migration. *Frontiers in Cell and Developmental Biology*, *8*, 549.

Lohmann, W., Schill, W. B., Bucher, D., Peters, T., Nilles, M., Schulz, A., & Bohle, R. (1994). Elastosis and cancer. *Zeitschrift fur Naturforschung. C, Journal of Biosciences*, *49*(3–4), 223–229.

Long, M. M., King, V. J., Prasad, K. U., & Urry, D. W. (1988). Chemotaxis of fibroblasts toward nonapeptide of elastin. *Biochimica Et Biophysica Acta*, *968*(3), 300–311.

Ludwig, N., Yerneni, S. S., Azambuja, J. H., Pietrowska, M., Widłak, P., Hinck, C. S., Głuszko, A., Szczepański, M. J., Kärmer, T., Kallinger, I., Schulz, D., Bauer, R. J., Spanier, G., Spoerl, S., Meier, J. K., Ettl, T., Razzo, B. M., Reichert, T. E., Hinck, A. P., & Whiteside, T. L. (2022). TGFβ+ small extracellular vesicles from head and neck squamous cell carcinoma cells reprogram macrophages towards a pro-angiogenic phenotype. *Journal of Extracellular Vesicles*, *11*(12), e12294.

Mahon, M. J. (2011). pHluorin2: An enhanced, ratiometric, pH-sensitive green florescent protein. *Advances in Bioscience and Biotechnology*, *2*(3), 132–137.

Maquart, F. X., Siméon, A., Pasco, S., & Monboisse, J. C. (1999). Régulation de l'activité cellulaire par la matrice celulaire: le concept de matrikines [Regulation of cell activity by the extracellular matrix: The concept of matrikines]. *Journal De La Societe De Biologie*, *193*(4–5), 423–428.

Mathieu, M., Martin-Jaular, L., Lavieu, G., & Théry, C. (2019). Specificities of secretion and uptake of exosomes and other extracellular vesicles for cell-to-cell communication. *Nature Cell Biology*, *21*(1), 9–17.

Nannan, L., Gsell, W., Belderbos, S., Gallet, C., Wouters, J., Brassart-Pasco, S., Himmelreich, U., & Brassart, B. (2023). A multimodal imaging study to highlight elastin-derived peptide pro-tumoral effect in a pancreatic xenograft model. *British Journal of Cancer*, *128*(11), 2000–2012.

Nguyen, V. V. T., Ye, S., Gkouzioti, V., van Wolferen, M. E., Yengej, F. Y., Melkert, D., Siti, S., de Jong, B., Besseling, P. J., Spee, B., van der Laan, L. J. W., Horland, R., Verhaar, M. C., & van Balkom, B. W. M. (2022). A human kidney and liver organoid-based multi-organ-on-a-chip model to study the therapeutic effects and biodistribution of mesenchymal stromal cell-derived extracellular vesicles. *Journal of Extracellular Vesicles*, *11*(11), e12280.

Procacci, P., Moscheni, C., Sartori, P., Sommariva, M., & Gagliano, N. (2018). Tumor¯stroma cross-talk in human pancreatic ductal adenocarcinoma: A focus on the effect of the extracellular matrix on tumor cell phenotype and invasive potential. *Cells*, *7*(10), 158.

Rahib, L., Smith, B. D., Aizenberg, R., Rosenzweig, A. B., Fleshman, J. M., & Matrisian, L. M. (2014). Projecting cancer incidence and deaths to 2030: The unexpected burden of thyroid, liver, and pancreas cancers in the United States. *Cancer Research*, *74*(11), 2913–2921.

Raposo, G., & Stoorvogel, W. (2013). Extracellular vesicles: Exosomes, microvesicles, and friends. *The Journal of Cell Biology*, *200*(4), 373–383.

Robinet, A., Fahem, A., Cauchard, J. H., Huet, E., Vincent, L., Lorimier, S., Antonicelli, F., Soria, C., Crepin, M., Hornebeck, W., & Bellon, G. (2005). Elastin-derived peptides enhance angiogenesis by promoting endothelial cell migration and tubulogenesis through upregulation of MT1-MMP. *Journal of Cell Science*, *118*(Pt 2), 343–356.

Sarcar, B., Fang, B., Izumi, V., O Nunez Lopez, Y., Tassielli, A., Pratley, R., Jeong, D., Permuth, J. B., Koomen, J. M., Fleming, J. B., & Stewart, P. A. (2022). A comparative proteomics analysis identified differentially expressed proteins in pancreatic cancer-associated stellate cell small extracellular vesicles. *Molecular & Cellular Proteomics*, *21*(12), 100438.

Senior, R. M., Griffin, G. L., & Mecham, R. P. (1980). Chemotactic activity of elastin-derived peptides. *The Journal of Clinical Investigation*, *66*(4), 859–862.

Shapiro, S. D., Endicott, S. K., Province, M. A., Pierce, J. A., & Campbell, E. J. (1991). Marked longevity of human lung parenchymal elastic fibers deduced from prevalence of D-aspartate and nuclear weapons-related radiocarbon. *The Journal of Clinical Investigation*, *87*(5), 1828–1834.

Shi, Y., Gao, W., Lytle, N. K., Huang, P., Yuan, X., Dann, A. M., Ridinger-Saison, M., DelGiorno, K. E., Antal, C. E., Liang, G., Atkins, A. R., Erikson, G., Sun, H., Meisenhelder, J., Terenziani, E., Woo, G., Fang, L., Santisakultarm, T. P., Manor, U., … Hunter, T. (2019). Targeting LIF-mediated paracrine interaction for pancreatic cancer therapy and monitoring. *Nature*, *569*(7754), 131–135.

Shinoda, H., Shannon, M., & Nagai, T. (2018). Fluorescent proteins for investigating biological events in acidic environments. *International Journal of Molecular Sciences*, *19*(6), 1548.

Smyth, T. J., Redzic, J. S., Graner, M. W., & Anchordoquy, T. J. (2014). Examination of the specificity of tumor cell derived exosomes with tumor cells in vitro. *Biochimica Et Biophysica Acta*, *1838*(11), 2954–2965.

Takahashi, Y., Nishikawa, M., Shinotsuka, H., Matsui, Y., Ohara, S., Imai, T., & Takakura, Y. (2013). Visualization and in vivo tracking of the exosomes of murine melanoma B16-BL6 cells in mice after intravenous injection. *Journal of Biotechnology*, *165*(2), 77–84.

Taylor, D. D., & Gerçel-Taylor, C. (2005). Tumour-derived exosomes and their role in cancer-associated T-cell signalling defects. *British Journal of Cancer*, *92*(2), 305–311.

Toupance, S., Brassart, B., Rabenoelina, F., Ghoneim, C., Vallar, L., Polette, M., Debelle, L., & Birembaut, P. (2012). Elastin-derived peptides increase invasive capacities of lung cancer cells by post-transcriptional regulation of MMP-2 and uPA. *Clinical & Experimental Metastasis*, *29*(5), 511–522.

Vania, L., Morris, G., Otgaar, T. C., Bignoux, M. J., Bernert, M., Burns, J., Gabathuse, A., Singh, E., Ferreira, E., & Weiss, S. F. T. (2019). Patented therapeutic approaches targeting LRP/LR for cancer treatment. *Expert Opinion on Therapeutic Patents*, *29*(12), 987–1009.

Verweij, F. J., Balaj, L., Boulanger, C. M., Carter, D. R. F., Compeer, E. B., D'Angelo, G., El Andaloussi, S., Goetz, J. G., Gross, J. C., Hyenne, V., Krämer-Albers, E. M., Lai, C. P., Loyer, X., Marki, A., Momma, S., Nolte-'t Hoen, E. N. M., Pegtel, D. M., Peinado, H., … van Niel, G. (2021). The power of imaging to understand extracellular vesicle biology in vivo. *Nature Methods*, *18*(9), 1013–1026.

Verweij, F. J., Bebelman, M. P., Jimenez, C. R., Garcia-Vallejo, J. J., Janssen, H., Neefjes, J., Knol, J. C., de Goeij-de Haas, R., Piersma, S. R., Baglio, S. R., Verhage, M., Middeldorp, J. M., Zomer, A., van Rheenen, J., Coppolino, M. G., Hurbain, I., Raposo, G., Smit, M. J., Toonen, R. F. G., … Pegtel, D. M. (2018). Quantifying exosome secretion from single cells reveals a modulatory role for GPCR signaling. *The Journal of Cell Biology*, *217*(3), 1129–1142.

Verweij, F. J., Revenu, C., Arras, G., Dingli, F., Loew, D., Pegtel, D. M., Follain, G., Allio, G., Goetz, J. G., Zimmermann, P., Herbomel, P., Del Bene, F., Raposo, G., & van Niel, G. (2019). Live tracking of inter-organ communication by endogenous exosomes in vivo. *Developmental Cell*, *48*(4), 573–589.e4.

Wiklander, O. P., Nordin, J. Z., O'Loughlin, A., Gustafsson, Y., Corso, G., Mäger, I., Vader, P., Lee, Y., Sork, H., Seow, Y., Heldring, N., Alvarez-Erviti, L., Smith, C. I., Le Blanc, K., Macchiarini, P., Jungebluth, P., Wood, M. J., & Andaloussi, S. E. (2015). Extracellular vesicle in vivo biodistribution is determined by cell source, route of administration and targeting. *Journal of Extracellular Vesicles*, *4*, 26316.

Williams, C., Palviainen, M., Reichardt, N. C., Siljander, P. R., & Falcón-Pérez, J. M. (2019). Metabolomics applied to the study of extracellular vesicles. *Metabolites*, *9*(11), 276.

Wu, A. Y., Sung, Y. C., Chen, Y. J., Chou, S. T., Guo, V., Chien, J. C., Ko, J. J., Yang, A. L., Huang, H. C., Chuang, J. C., Wu, S., Ho, M. R., Ericsson, M., Lin, W. W., Cheung, C. H. Y., Juan, H. F., Ueda, K., Chen, Y., & Lai, C. P. (2020). Multiresolution imaging using bioluminescence resonance energy transfer identifies distinct biodistribution profiles of extracellular vesicles and exomeres with redirected tropism. *Advanced Science*, *7*(19), 2001467.

Wu, Y., Tan, X., Liu, P., Yang, Y., Huang, Y., Liu, X., Meng, X., Yu, B., Wu, M., & Jin, H. (2019). ITGA6 and RPSA synergistically promote pancreatic cancer invasion and metastasis via PI3K and MAPK signaling pathways. *Experimental Cell Research*, *379*(1), 30–47.

Xu, L., Faruqu, F. N., Liam-Or, R., Abu Abed, O., Li, D., Venner, K., Errington, R. J., Summers, H., Wang, J. T., & Al-Jamal, K. T. (2020). Design of experiment (DoE)-driven *in vitro* and *in vivo* uptake studies of exosomes for pancreatic cancer delivery enabled by copper-free click chemistry-based labelling. *Journal of Extracellular Vesicles*, *9*(1), 1779458.

Zaborowski, M. P., Cheah, P. S., Zhang, X., Bushko, I., Lee, K., Sammarco, A., Zappulli, V., Maas, S. L. N., Allen, R. M., Rumde, P., György, B., Aufiero, M., Schweiger, M. W., Lai, C. P., Weissleder, R., Lee, H., Vickers, K. C., Tannous, B. A., & Breakefield, X. O. (2019). Membrane-bound Gaussia luciferase as a tool to track shedding of membrane proteins from the surface of extracellular vesicles. *Scientific Reports*, *9*(1), 17387.

Zhu, L., Gangadaran, P., Kalimuthu, S., Oh, J. M., Baek, S. H., Jeong, S. Y., Lee, S. W., Lee, J., & Ahn, B. C. (2018). Novel alternatives to extracellular vesicle-based immunotherapy—exosome mimetics derived from natural killer cells. *Artificial Cells, Nanomedicine, and Biotechnology*, *46*(sup3), S166–S179.

SUPPORTING INFORMATION

Additional supporting information can be found online in the Supporting Information section at the end of this article.